Modeling of PWM Boost Converters for Continuous and Discontinuous Inductor Current Modes

By Jie Qiu

Supervised by Dr. Krishnamoorthy Natarajan

December, 2005

A Thesis submitted in partial fulfillment of the requirements of

the Msc. Eng. Degree in

Control Engineering

Faculty of Engineering

Lakehead University

Thunder Bay, Ontario

Library and
Archives Canada

Bibliothèque et
Archives Canada

Published Heritage
Branch

Direction du
Patrimoine de l'édition

395 Wellington Street
Ottawa ON K1A 0N4
Canada

395, rue Wellington
Ottawa ON K1A 0N4
Canada

NOTICE:
The author has granted a non-exclusive license allowing Library and Archives Canada to reproduce, publish, archive, preserve, conserve, communicate to the public by telecommunication or on the Internet, loan, distribute and sell theses worldwide, for commercial or non-commercial purposes, in microform, paper, electronic and/or any other formats.

AVIS:
L'auteur a accordé une licence non exclusive permettant à la Bibliothèque et Archives Canada de reproduire, publier, archiver, sauvegarder, conserver, transmettre au public par télécommunication ou par l'Internet, prêter, distribuer et vendre des thèses partout dans le monde, à des fins commerciales ou autres, sur support microforme, papier, électronique et/ou autres formats.

The author retains copyright ownership and moral rights in this thesis. Neither the thesis nor substantial extracts from it may be printed or otherwise reproduced without the author's permission.

L'auteur conserve la propriété du droit d'auteur et des droits moraux qui protège cette thèse. Ni la thèse ni des extraits substantiels de celle-ci ne doivent être imprimés ou autrement reproduits sans son autorisation.

In compliance with the Canadian Privacy Act some supporting forms may have been removed from this thesis.

Conformément à la loi canadienne sur la protection de la vie privée, quelques formulaires secondaires ont été enlevés de cette thèse.

While these forms may be included in the document page count, their removal does not represent any loss of content from the thesis.

Bien que ces formulaires aient inclus dans la pagination, il n'y aura aucun contenu manquant.

Canada

Abstract

Owing to the relatively more complicated nature of the boost converter with non-ideal elements and operating in continuous and discontinuous inductor current modes, a parsimonious large signal and small signal model for this converter, with and without feedback, has been lacking. In this work, a zero order hold equivalent discrete time model of the boost converter for computing its small signal frequency response and large signal and small signal closed loop behavior is developed and experimentally confirmed. The Newton-Raphson technique is used to accelerate the computation of the frequency response from the developed discrete time model. The use of the discrete time model in combination with the Newton-Raphson method in predicting the steady-state ripple behavior of the converter is also studied. With the intention of future robust control studies on the boost converter in discontinuous inductor current mode, an initial evaluation of the frequency response predicted by the discrete time model at different operating points is presented.

i

Acknowledgment

Dr. K. Natarajan's extreme help and guidance made this work possible. I sincerely appreciate his help and support.

ii

Contents

verter   **20**

List of Figures

vii

List of Tables

Chapter 1

Introduction

1.1 The overview of literature

Various linear time-invariant models for boost converters in continuous inductor current mode of operation such as state-space averaged models [1], [2] and the PWM switch model [3] have been developed and they yield similar results. When the boost converter operates in continuous and discontinuous inductor current operation modes, owing to the relatively more complicated nature of the boost converter with non-ideal elements, a parsimonious large signal and small signal model for this converter, with and without feedback, has been lacking. Firstly, linear time-invariant small signal state-space averaged model [4] and the PWM switch model [5] with ideal elements were developed and it was observed that [5] yields results which are different from those given by the method of [4]. The fundamental difference between the two methods is that state-space averaged model predicts that the discontinuous current state does not contribute to the order of the average model while the PWM switch model predicts otherwise. Later, a small-signal circuit model of DC-DC PWM boost converters operating in discontinuous inductor current mode [6] was derived by using the energy conservation approach [7], [8] to consider some of the non-ideal effects and [6] verified the results in [5]. For robust controller design purpose, the converter closed loop behavior is often governed by the presence of both

1

continuous and discontinuous inductor current modes. Consequently a model which can handle both continuous and discontinuous inductor current modes easily is needed. In this thesis, a zero-order hold (ZOH) equivalent discrete time model of the boost converter for computing its small signal frequency response and closed loop behavior for both large and small signals is derived and experimentally confirmed. In this model, non-ideal effects can be easily taken into account in continuous and discontinuous inductor current modes. Earlier work done by [9] indicates that this approach can handle both continuous and discontinuous inductor current modes in the buck converter. In discontinuous inductor current mode, the use of the discrete time model in combination with a two variable Newton-Raphson technique with analytical Jacobian in predicting steady-state behavior is also studied. For robust controller design, ZOH modeling of state-space descriptions has the potential of developing frequency response characteristics which are obtained from the developed model of this thesis.

1.2   Thesis outline

The organization of the thesis is as follows. Chapter 1 provides an introduction to the basic concept of the boost converter. In Chapter 2 two kinds of models are introduced. The models include C-code based simulation model and a discrete-time model, which is a ZOH model of the boost converter for both continuous and discontinuous modes of operation. In Chapter 3 the behavior of the models of Chapter 2 are observed, compared and experimentally verified in terms of steady-state and small signal frequency response. An alternative faster method using Newton-Raphson technique to accelerate the computation of frequency response from the developed discrete-time model is introduced. In Chapter 4, this discrete-time model is used to predict large signal and small signal behavior when the converter is working in closed-loop with an analog PI controller. Experimental results of such large signal behavior are presented and compared to results predicted from this discrete-time model of Chapter 2. In Chapter 5, on the basis of Chapters 3 and 4, the

2

behavior of the discrete-time model over different operating points is also obtained and experimentally confirmed. Chapter 6 suggests future work and concludes the thesis.

1.3 Switch mode DC-DC converters

Switch mode DC-DC power converters afford an efficient means of transforming power at one DC voltage to another desired DC voltage. The basic DC-DC conversion function is achieved by controlling the switch on and off durations with constant switching frequency. Compared with linear power supply, it has greater efficiency.

1.4 Step-up (boost) converter

As the name implies, a boost converter produces an average output voltage V_o always greater than the DC input voltage V_d. Fig. 1-1 shows an ideal boost converter circuit. When the switch is on, the diode is reversed biased, thus isolating the output stage. The input supplies energy to the inductor. When the switch is off, the output stage receives energy from the inductor as well as from the input. The output filter essentially guarantees a relatively low ripple voltage on the load.

1.5 Control of boost converter

The output voltages V_o of DC power supplies are regulated to be within a specified tolerance band (e.g., $\pm 1\%$ around its nominal value) in response to changes in the output load R_{load} and input line voltage V_d. This is accomplished by using a negative-feedback control system, shown in Fig. 1-2. One of the methods for controlling the output voltage, called Pulse-width modulation (PWM) switching, employs switching at a constant switching frequency and adjusting the on duration of the switch in order to ensure $V_o = V_{ref}$.

3
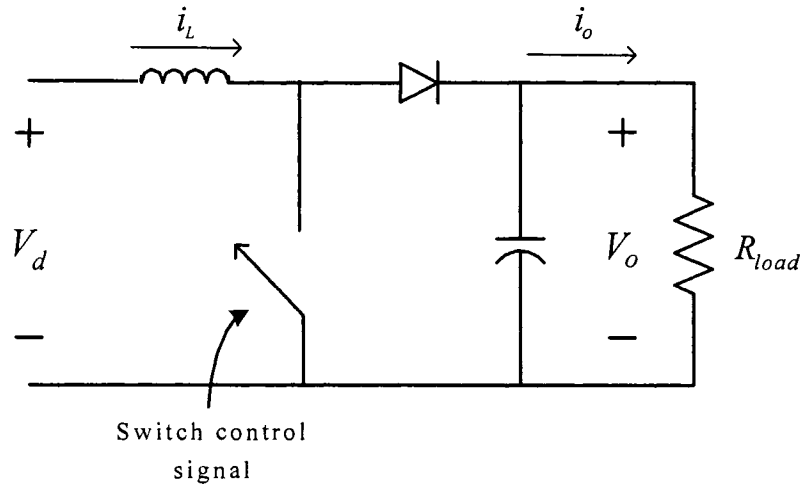
Figure 1-1: Boost converter

Duty cycle of the switch control signal is generated by comparing a control voltage signal $v_{control}$ which is the output of the PI controller with a repetitive saw-tooth waveform of amplitude $\widehat{V}_{st}$ as shown in Fig. 1-2. The frequency $f_s(=\frac{1}{T_s})$ and amplitude $\widehat{V}_{st}$ of the saw-tooth waveform are constant. In terms of $v_{control}$ and the amplitude of the saw-tooth waveform $\widehat{V}_{st}$ in Fig. 1-2, the duty cycle of the switch control signal can be expressed as

$$d = \frac{v_{control}}{\widehat{V}_{st}} \tag{1.1}$$

1.6 Modes of operation

The operation of this converter can be divided into two modes according to ideal inductor current waveform. If the inductor current never falls to zero over a switching period, the converter is said to be working in *continuous − conduction mode* of operation as in Fig. 1-3.(a). If the inductor current becomes zero for a portion in the switch off (t_{off}) period as in Fig. 1-3.(b), then the converter is working in *discontinuous − conduction mode*. At

4
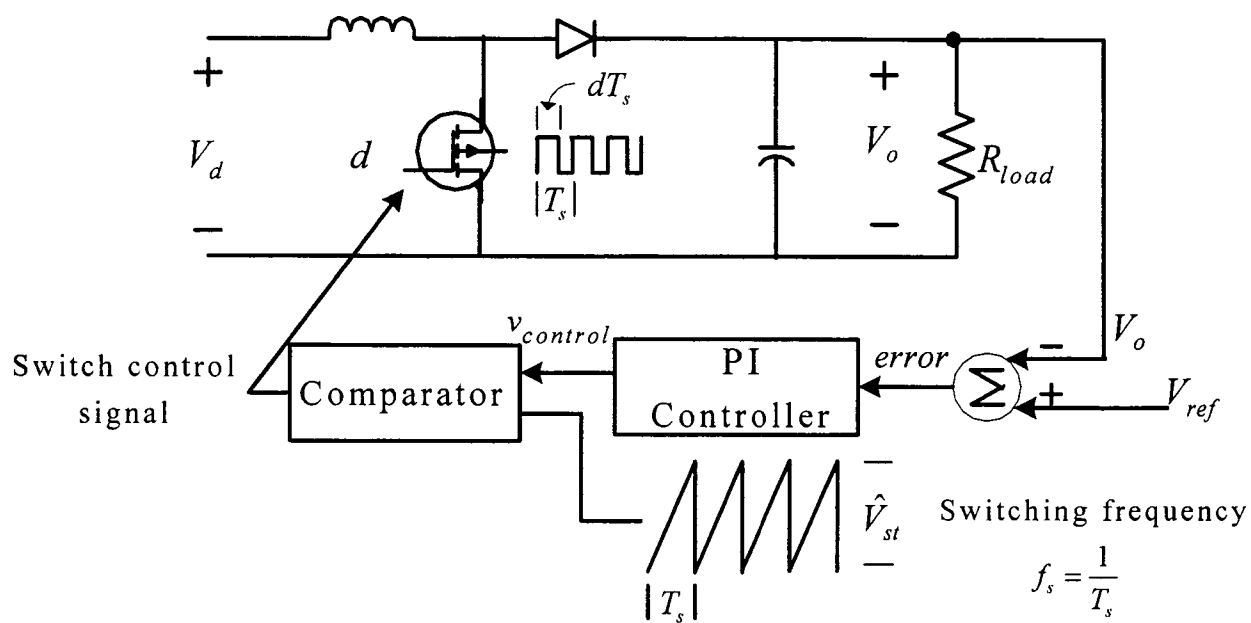
Figure 1-2: Controller circuit of a boost converter

(a) Inductor voltage and current
in continuous-conduction mode

(b) Inductor voltage and current
in discontinuous-conduction mode
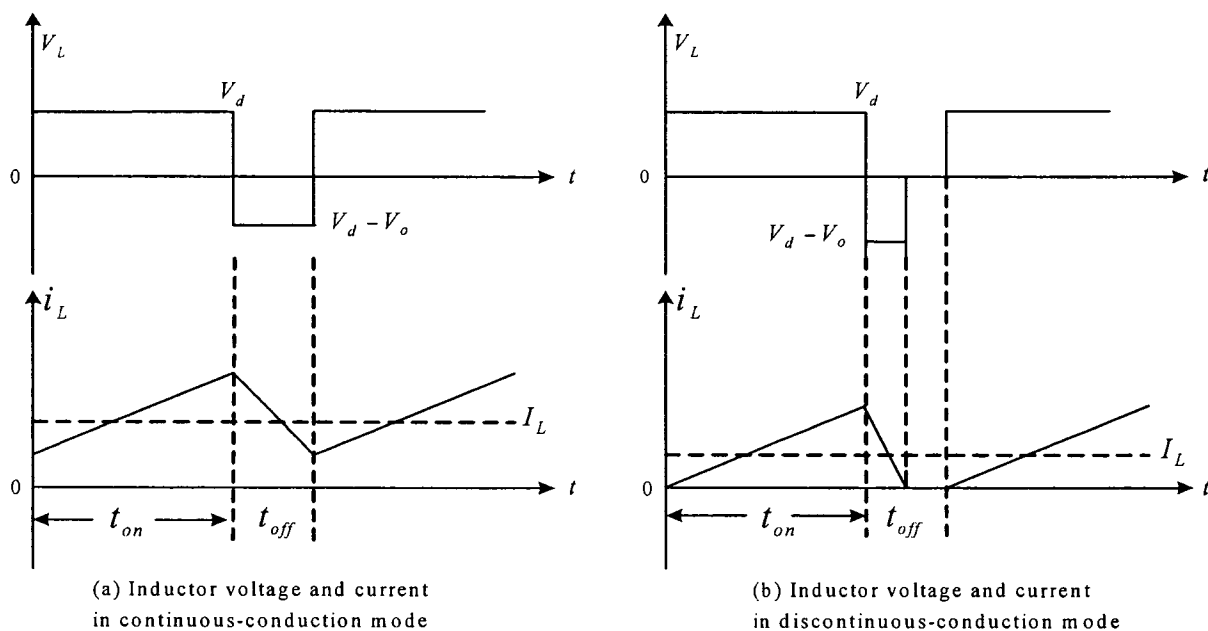
Figure 1-3: Inductor voltage and current

5

the boundary between continuous and discontinuous mode, inductor current goes to zero exactly at the end of t_{off}. At this boundary, in the boost converter with ideal elements, the average inductor current is [1]

$$I_{LB} = \frac{1}{2}\frac{V_d}{L}t_{on} = \frac{T_s V_o}{2L}d(1 - d) \tag{1.2}$$

Recognizing that in a boost converter the inductor current and the input current are the same ($i_d = i_L$) and using above equation, we find that average output current at the boundary condition is

$$I_{oB} = \frac{T_s V_o}{2L}d(1 - d)^2 \tag{1.3}$$

and I_{oB} has its maximum value at $d = \frac{1}{3} = 0.333$ given by,

$$I_{oB, \text{ max}} = \frac{2}{27}\frac{T_s V_o}{L} = 0.074\frac{T_s V_o}{L} \tag{1.4}$$

Therefore, if the average load current drops below I_{oB} (and, hence, the average inductor current below I_{LB}), the inductor current will enter discontinuous-conduction mode else it is in continuous-conduction mode for the ideal boost converter.

6

Chapter 2

Models of the boost converter

In this chapter, a new discrete time model of the non-ideal boost converter for computing its standalone behavior in terms of steady-state and small signal frequency-response is developed. In Section 2.1, the basic differential equations of the boost converter are derived. The models discussed in following sections are all based on these equations.

2.1 Differential equations of a boost converter

Fig. 2-1 shows the topology of the boost converter. The non-ideal elements of the converter are modeled as r_L for the inductor resistance and r_c for the capacitor equivalent series resistance (ESR). Furthermore, to more accurately model the system, the switch and diode are not considered as ideal components.

The non-ideal effects (conduction losses) induced by the switch and diode are taken into account as follows:

1) The MOSFET in the ON state is modeled by a linear resistance r_{DS} and in the OFF state by an infinite resistance.

2) The diode in the ON state is modeled by a linear voltage drop V_F and a resistance r_F. The diode in the OFF state is modeled as an infinite resistance.

Implicit switching losses induced by the switch and diode can also be modeled by

7
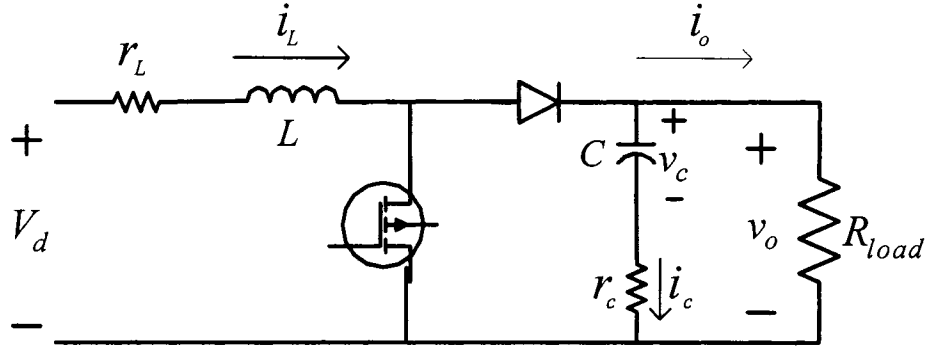
Figure 2-1: Boost converter circuit

adjusting the values of the non-ideal elements as above. It is assumed that when the switch is on, the diode is off and when the switch is off, the diode is on.

There are two topological modes for continuous conduction mode and three for discontinuous conduction mode. Fig. 2-2 shows the three topological modes of the boost converter operating in the discontinuous-conduction mode. The first two topological modes shown in Fig. 2-2 illustrate the modes in the continuous-conduction mode. The following equations can be derived based on Fig. 2-2,

For (I):

$$-V_d + (r_L + r_{DS})i_L(t) + L\frac{di_L(t)}{dt} = 0 \tag{2.1}$$

$$-v_c(t) - C\frac{dv_c(t)}{dt}r_c + v_o(t) = 0 \tag{2.2}$$

$$v_o(t) = -R_{load}C\frac{dv_c(t)}{dt} \tag{2.3}$$

For (II):

$$-V_d + (r_L + r_F)i_L(t) + L\frac{di_L(t)}{dt} + V_F + v_o(t) = 0 \tag{2.4}$$

8
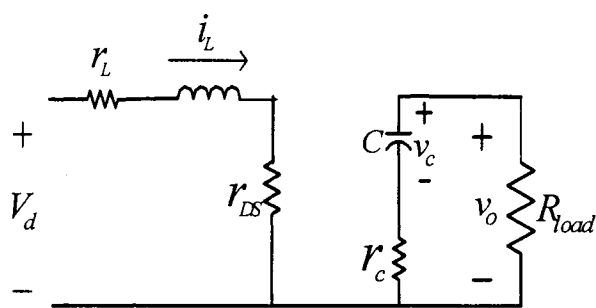
(I). Switch on; Diode off
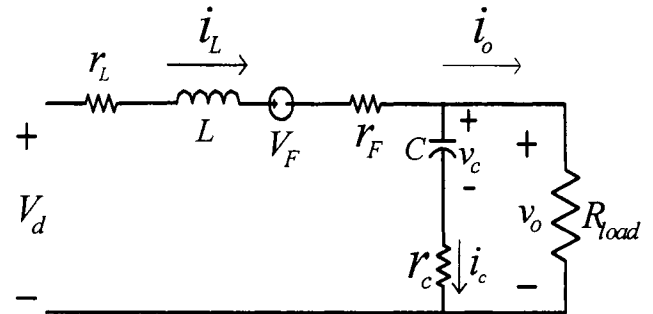
(II). Switch off; Diode on
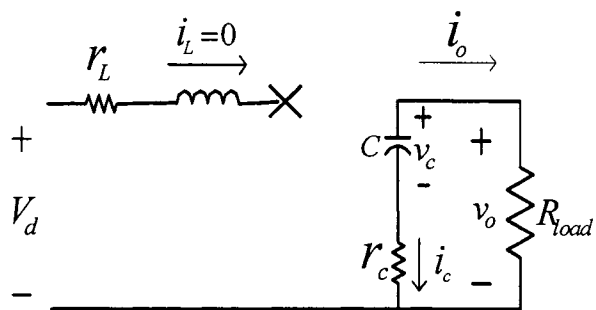
(III). Switch off; Diode off

Figure 2-2: Three topological modes of the boost converter operating in discontinuous-conduction mode

9

$$-v_c(t) - C\frac{dv_c(t)}{dt}r_c + v_o(t) = 0 \tag{2.5}$$

$$v_o(t) = R_{load}\left(i_L(t) - C\frac{dv_c(t)}{dt}\right) \tag{2.6}$$

For (III):

$$i_L(t) = 0 \tag{2.7}$$

$$-v_c(t) - C\frac{dv_c(t)}{dt}r_c + v_o(t) = 0 \tag{2.8}$$

$$v_o(t) = -R_{load}C\frac{dv_c(t)}{dt} \tag{2.9}$$

where i_L is the inductor current, v_c is the capacitor voltage and v_o is the voltage across the load. For the boost converter topology shown in Fig. 2-1, the differential equations governing the converter for modes I and II are written in matrix form as:

$$\begin{bmatrix} \frac{di_L(t)}{dt} \\ \frac{dv_c(t)}{dt} \end{bmatrix} = A(S)\begin{bmatrix} i_L(t) \\ v_c(t) \end{bmatrix} + B(S); \qquad v_o(t) = C(S)\begin{bmatrix} i_L(t) \\ v_c(t) \end{bmatrix} \tag{2.10}$$

where S, ($\bar{S}$) is an integer variable which is 1, (0) if the switch is on and 0, (1) if the switch is off. The matrices $A(S)$, $B(S)$, $C(S)$ are given by:

$$A(S) = \begin{bmatrix} -\frac{r_L + Sr_{DS} + \bar{S}r_F}{L} - \bar{S}\frac{R_{load}r_c}{L(r_c + R_{load})} & -\bar{S}\frac{R_{load}}{L(r_c + R_{load})} \\ \bar{S}\frac{R_{load}}{C(r_c + R_{load})} & -\frac{1}{C(r_c + R_{load})} \end{bmatrix} \tag{2.11}$$

$$B(S) = \begin{bmatrix} \frac{V_d - \bar{S}V_F}{L} \\ 0 \end{bmatrix}; \qquad C(S) = \begin{bmatrix} \bar{S}\frac{R_{load}r_c}{r_c + R_{load}} & \frac{R_{load}}{r_c + R_{load}} \end{bmatrix} \tag{2.12}$$

During discontinuous-conduction mode of operation, for $i_L = 0$, both switch and diode are off and (2.10) reduces to

$$\frac{dv_c(t)}{dt} = -\frac{1}{C(r_c + R_{load})}v_c(t) \tag{2.13}$$

10

The output equation, for this case, remains the same as in (2.10) with $i_L(t) = 0$.

2.2 Discrete-time model

A new ZOH discrete-time model developed in this thesis is introduced here. Small-signal model [6] assumes that the perturbations are very small and converter always works in discontinuous-conduction mode or continuous-conduction mode. However for large perturbations on nominal operating point, converter will not operate in discontinuous mode only but will exhibit both continuous and discontinuous modes of operation. So the discrete-time model is developed based on both modes of operation and predicts the behavior of the converter (with and without feedback) in both modes.

2.2.1 Discrete time model

In the development of the discrete-time model, the following assumptions are made:

The duty cycle d ($0 \leq d \leq 1$) of the switch can be affected only once every switching period T_s and the switching frequency is higher than the resonant frequency of the main inductor and capacitor of the circuit. Since in practice the switching periods are being pushed to smaller values, this assumption is reasonable to make for modeling purposes.

At intervals of switching period the evolution of the state vector $x = \begin{bmatrix} i_L(t) & v_c(t) \end{bmatrix}'$ for all three modes of Fig. 2-2 is described by:

$$x_{(k+d_k)T_s} = F_1 x_{kT_s} + G_1 \qquad \text{during switch on:} \quad d_k T_s \qquad (2.14)$$

$$x_{(k+1)T_s} = F_3 F_2 x_{(k+d_k)T_s} + F_3 G_2 \qquad \text{during switch off:} \quad (1 - d_k)T_s \quad (2.15)$$

where F_1, F_2, F_3, the state transition matrices, and G_1, G_2 are obtained as per:

$$F_1 = e^{A(1)d_k T_s} \qquad G_1 = (F_1 - I)A(1)^{-1}B(1) \qquad (2.16)$$

11
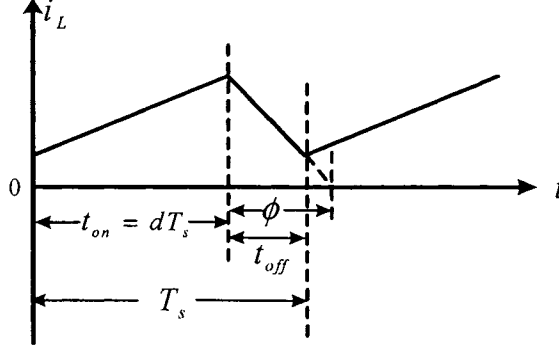
Figure 2-3: Inductor current and ϕ in continuous-conduction mode

$$F_2 = e^{A(0)(1-d_k)T_s} \qquad \text{if} \quad \phi_k \geq (1 - d_k)T_s \tag{2.17}$$

$$F_2 = e^{A(0)\phi_k} \qquad \text{if} \quad \phi_k < (1 - d_k)T_s \tag{2.18}$$

$$G_2 = (F_2 - I)A(0)^{-1}B(0) \tag{2.19}$$

$$F_3 = I \qquad \text{if} \quad \phi_k \geq (1 - d_k)T_s \tag{2.20}$$

$$F_3 = \begin{bmatrix} 1 & 0 \\ 0 & e^{a_{22}((1-d_k)T_s - \Phi_k)} \end{bmatrix} \qquad \text{if} \quad \phi_k < (1 - d_k)T_s \tag{2.21}$$

where k is an integer that indexes the switching periods. In (2.21), a_{22} is the element in the second row and second column in the $A(S)$ matrix given in (2.11, 2.13) and ϕ_k is the time duration taken by inductor current i_L to become zero after the switch is opened at time $(k + d_k)T_s$. If $\phi_k < (1 - d_k)T_s$, then the converter is in discontinuous-conduction mode else it is in continuous-conduction mode.

The terms, F_2, G_2, F_3, and ϕ_k will be explained and derived in the next section.

2.2.2 Calculations of F_2, G_2 and F_3

As seen from Figs. 2-3 and 2-4, two states in the t_{off} interval can be distinguished: one when inductor current flows ($i_L > 0$, diode is on) up to the end of the switching period and one when inductor current goes to zero before the end of the switching period

12
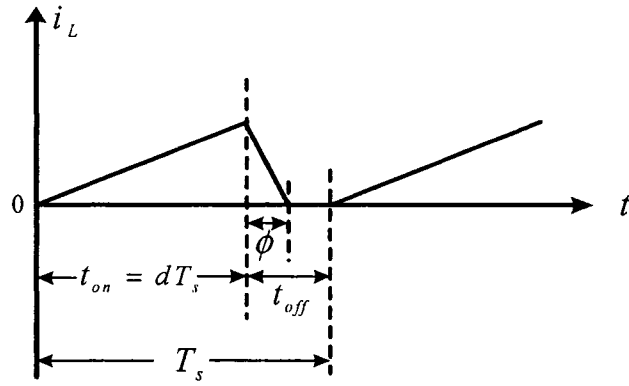
Figure 2-4: Inductor current and ϕ in discontinuous-conduction mode

($i_L = 0$, diode is off).

As seen in Fig. 2-3, if $\phi \geq t_{off}$, which means the inductor current flows during t_{off}, the converter is working in continuous-conduction mode. Thus, F_2 and F_3 in (2.15) are obtained as (2.17) and (2.20).

However, Fig. 2-4 illustrates the situation for $\phi < t_{off}$. When the inductor current is zero for some duration in the t_{off} interval, the boost converter is working in discontinuous-conduction mode. In this case, during the ϕ_k interval, when $i_L > 0$, F_2, G_2 in (2.15) are calculated as,

$$F_2 = e^{A(0)\phi_k}$$

$$G_2 = (F_2 - I)A(0)^{-1}B(0)$$

For the remaining part of the t_{off} interval, which is $(1 - d_k)T_s - \phi_k$, the equations for $i_L = 0$ are applied and F_3 in (2.15) is calculated as,

$$F_3 = e^{A((1-d_k)T_s - \phi_k)} \tag{2.22}$$

13

With (2.7) holding in this interval and switch and diode off, the matrix (2.11) reduces to

$$A = \begin{bmatrix} 0 & 0 \\ 0 & -\frac{1}{C(r_c + R_{load})} \end{bmatrix} \tag{2.23}$$

Substituting (2.23) in (2.22), gives

$$F_3 = \begin{bmatrix} 1 & 0 \\ 0 & e^{a_{22}((1-d_k)T_s - \phi_k)} \end{bmatrix}$$

where $a_{22} = -\frac{1}{C(r_c + R_{load})}$. Thus (2.14), (2.15) in discontinuous-conduction mode are obtained as:

$$x_{(k+d_k)T_s} = F_1 x_{kT_s} + G_1 \tag{2.24}$$

$$x_{(k+d_k)T_s + \phi_k} = F_2 x_{(k+d_k)T_s} + G_2 \tag{2.25}$$

$$x_{(k+1)T_s} = F_3 x_{(k+d_k)T_s + \phi_k} \tag{2.26}$$

Substituting $x_{(k+d_k)T_s}$ from (2.24) into (2.25) and $x_{(k+d_k)T_s + \phi_k}$ from (2.25) into (2.26),

$$x_{(k+1)T_s} = F_3 F_2 F_1 x_{kT_s} + F_3 F_2 G_1 + F_3 G_2 \tag{2.27}$$

2.2.3 Equation for ϕ

Fig. 2-4 shows that while the t_{on} interval (dT_s) is a known quantity (at least for open-loop case), the ϕ interval is as yet unknown and depends in general on both the length of the t_{on} interval and other circuit parameters, and how deep in discontinuous or continuous conduction mode the converter is operating. Hence, determining this unknown quantity ϕ becomes an exigent problem. Unlike [9] however, the equation solving for ϕ is implicit and can be derived using the eigenvalue and corresponding eigenvector matrix of $A(0)$. Multiplying (2.25) by a matrix $C = \begin{bmatrix} 1 & 0 \end{bmatrix}$ to obtain the inductor current which goes

14

to zero at the end of the ϕ interval, the following equation is obtained:

$$Cx_{(k+d_k)T_s+\phi_k} = \begin{bmatrix} 1 & 0 \end{bmatrix} \begin{bmatrix} i_{L_{(k+d_k)T_s+\phi_k}} \\ \\ v_{C_{(k+d_k)T_s+\phi_k}} \end{bmatrix} = i_{L_{(k+d_k)T_s+\phi_k}} = 0$$

Substituting (2.18, 2.19) in above equation, gives

$$Ce^{A(0)\phi_k}x_{(k+d_k)T_s} + C(e^{A(0)\phi_k} - I)A(0)^{-1}B(0) = 0 \tag{2.28}$$

Using the eigenvector and eigenvalue decomposition of $A(0)$ with T denoting the eigenvector matrix and Λdenoting the diagonal eigenvalue matrix, the following equation is obtained,

$$A(0)T = T\Lambda$$

from which

$$A(0) = T\Lambda T^{-1}$$

matrix exponential $e^{A(0)\phi_k}$ is now given by [10]:

$$e^{A(0)\phi_k} = Te^{\Lambda\phi_k}T^{-1}$$

then (2.28) becomes

$$(CT)e^{\Lambda\phi_k}(T^{-1}x_{(k+d_k)T_s}) + (CT)e^{\Lambda\phi_k}\Lambda^{-1}T^{-1}B(0) - (CT)\Lambda^{-1}T^{-1}B(0) = 0 \tag{2.29}$$

If the eigenvalues of $A(0)$ are λ_1, λ_2, (2.29) can be simplified as follows:

$$(CT)\begin{bmatrix} e^{\lambda_1\phi_k} & 0 \\ \\ 0 & e^{\lambda_2\phi_k} \end{bmatrix} \begin{bmatrix} T^{-1}x_{(k+d_k)T_s} + \Lambda^{-1}T^{-1}B(0) \end{bmatrix} = (CT)\Lambda^{-1}T^{-1}B(0) \Longrightarrow$$

15

$$(t_{11} \quad t_{12}) \begin{bmatrix} e^{\lambda_1 \phi_k} & 0 \\ 0 & e^{\lambda_2 \phi_k} \end{bmatrix} \begin{bmatrix} \frac{t_{22}}{\Delta} i_{L_{(k+d_k)T_s}} - \frac{t_{12}}{\Delta} v_{c_{(k+d_k)T_s}} + B_{11}(0) \frac{t_{22}}{\lambda_1 \Delta} \\ -\frac{t_{21}}{\Delta} i_{L_{(k+d_k)T_s}} + \frac{t_{11}}{\Delta} v_{c_{(k+d_k)T_s}} - B_{11}(0) \frac{t_{21}}{\lambda_2 \Delta} \end{bmatrix}$$

$$= (t_{11} \quad t_{12}) \begin{bmatrix} B_{11}(0) \frac{t_{22}}{\lambda_1 \Delta} \\ -B_{11}(0) \frac{t_{21}}{\lambda_2 \Delta} \end{bmatrix} \Longrightarrow$$

$$(t_{11} \quad t_{12}) \begin{bmatrix} e^{\lambda_1 \phi_k} \left(\frac{t_{22}}{\Delta} i_{L_{(k+d_k)T_s}} - \frac{t_{12}}{\Delta} v_{c_{(k+d_k)T_s}} + B_{11}(0) \frac{t_{22}}{\lambda_1 \Delta} \right) \\ e^{\lambda_2 \phi_k} \left(-\frac{t_{21}}{\Delta} i_{L_{(k+d_k)T_s}} + \frac{t_{11}}{\Delta} v_{c_{(k+d_k)T_s}} - B_{11}(0) \frac{t_{21}}{\lambda_2 \Delta} \right) \end{bmatrix}$$

$$= B_{11}(0) \left[\frac{t_{11} t_{22}}{\lambda_1 \Delta} - \frac{t_{12} t_{21}}{\lambda_2 \Delta} \right] \Longrightarrow$$

$$\alpha_1 e^{\lambda_1 \phi_k} + \alpha_2 e^{\lambda_2 \phi_k} = \alpha_3 \tag{2.30}$$

where

$$\alpha_1 = t_{11} \left(\frac{t_{22}}{\lambda_1} B_{11}(0) + t_{22} i_{L_{(k+d_k)T_s}} - t_{12} v_{c_{(k+d_k)T_s}} \right) \tag{2.31}$$

$$\alpha_2 = -t_{12} \left(\frac{t_{21}}{\lambda_2} B_{11}(0) + t_{21} i_{L_{(k+d_k)T_s}} - t_{11} v_{c_{(k+d_k)T_s}} \right) \tag{2.32}$$

$$\alpha_3 = B_{11}(0) \left(\frac{t_{11} t_{22}}{\lambda_1} - \frac{t_{12} t_{21}}{\lambda_2} \right) \tag{2.33}$$

In (2.31,2.32,2.33), t_{ij} are the elements of the eigenvector matrix T of $A(0)$ and $i_{L_{(k+d_k)T_s}}$, $v_{c_{(k+d_k)T_s}}$ are the inductor current and capacitor voltage when the switch is opened and are obtainable from (2.24).

2.2.4 Newton-Raphson method to compute ϕ

It can be seen from (2.30) that ϕ_k involves an exponential function and depends on previous state variables. To solve this equation, one of the most widely used methods of all root-locating formulas, the Newton-Raphson method from the Taylor series expansion [11] is used. This method is quadratically convergent. The root estimate is based on a

16

first order Taylor series expansion of a $n \times 1$ vector function $f(x_n)$ in x_n a $n \times 1$ vector. Suppose that $\bar{x}_n$ is the initial guess at the root and x_n is a better approximation.

$$f(x_n) = f(\bar{x}_n + \Delta x_n) \approx f(\bar{x}_n) + f'(\bar{x}_n)\Delta x_n$$

where $f'(\bar{x}_n)$ is a $n \times n$ Jacobian matrix of f at $\bar{x}_n$ and Δx_n denotes a $n \times 1$ increment vector.

$$f(x_n) = f(\bar{x}_n) + \left[\begin{array}{ccc} \frac{\partial f}{\partial x_1}(\bar{x}) & \cdots & \frac{\partial f}{\partial x_n}(\bar{x}) \end{array} \right] \Delta x_n \qquad (2.34)$$

Instead of solving $f(x_n) = 0$ directly, which is usually impossible, linearized equation (2.34) can be solved at $\bar{x}_n$ and rearranged to yield

$$\Delta x_n = - \left[f'(\bar{x}_n) \right]^{-1} f(\bar{x}_n); \quad f'(\bar{x}_n) = \left[\begin{array}{ccc} \frac{\partial f}{\partial x_1}(\bar{x}) & \cdots & \frac{\partial f}{\partial x_n}(\bar{x}) \end{array} \right] \qquad (2.35)$$

which is the Newton-Raphson formula. This will be used for solving two variables problem in Section 3.1.2 later in which both f and x are vectors of type 2×1. In numerical computation, the scalar version of the method when applied to (2.30) is found to converge to the final value of ϕ_k typically in four iterations with a tolerance of 10^{-11}. This shows that (2.30) in combination with Newton-Raphson method can be used to efficiently compute ϕ for both transient and steady-state analysis.

2.3 C-code based simulation model

Based on differential equations of the boost converter in Section 2.1, a straightforward modeling technique, albeit computationally intensive, to obtain instantaneous values of inductor current, capacitor voltage and any other desired variable in the circuit is to solve the differential equations of the boost converter numerically in small time-steps.

This is accomplished using C programming language with Fig. 1-2 as the schematic diagram in this thesis and serves to cross check results from the discrete-time model by

17

detailed simulation. While other general circuit simulation technique/program such as PSpice and MATLAB/Simulink etc. may be used to simulate the boost converter, C-code provides complete control of the simulation. For crosschecking, the code is needed in two forms as detailed in Section 2.3.1 and Section 2.3.2.

2.3.1 Open-loop boost converter operation

In order to find frequency-response of the boost converter, the boost converter in stand-alone (open-loop) mode is simulated. The input control signal $v_{control}$ (Fig. 1-2) is composed of a given DC input bias and a small sinusoidal variation whose input amplitude can be given directly with the controller portion of the program turned off. At each time step, the simulation program does the following:

- Determines the status of the switch comparing the control signal $v_{control}$ with a saw-tooth waveform generated in the program.

- Updates values of inductor current i_L, capacitor voltage v_c and output voltage v_o by solving the differential equations in Section 2.1 at each time step, using a fourth-order Runge-Kutta method.

2.3.2 Closed-loop boost converter operation

In closed-loop situation for a boost converter with respect to Fig. 1-2 the control signal $v_{control}$ is calculated using *error* at input of the PI controller rather than a directly given value and this *error* is obtained by subtracting the instantaneous output voltage v_o from V_{ref}.

For numerical precision, the time step of the code of Section 2.3.1 is set to $0.001\mu s$ which is equivalent 20,000 samples per switching period for a switching frequency of $f_s = 50kHz$. This time step was used to ensure accurate computation of frequency-response, particularly for phase shift calculation. For efficiency, the time step of the code of Section 2.3.2 is set to a bigger value ($0.005\mu s$), and there is no difference using the two different values of the time step in this case. The program is used to simulate the converter to

18

steady-state of output voltage and all data files obtained are processed in MATLAB for graphing/other analysis.

2.4 Conclusion

Two models of the boost converter are introduced in this chapter. C-code based simulation implemented in this thesis accurately simulates the system by considering very fine time-steps and calculating the state variables at each time step. Both continuous and discontinuous inductor current modes of operation can be detected using this simulation tool. This however involves a time-consuming numerical technique and is not compatible for analytical purposes.

A new discrete-time model (state space representation) is developed in Section 2.2. Non-ideal components have been taken into account through various parameters (r_L, r_c, r_{DS}, r_F, and V_F) in order to obtain more accurate results using this new model. Compared with existing modeling methods, the new discrete-time model developed in Section 2.2 not only includes the advantage of C-code based simulation but overcomes numerical inefficiency. By computing the frequency-response from this model (Chapter 3), it can be used for controller design and other purposes.

In the next chapter, the open-loop behavior of the models is considered through simulation and experimental results.

19

Chapter 3

Steady-state behavior and frequency-response analysis of the boost converter

In this chapter, the models of Chapter 2 are applied to a particular experimental boost converter with parameters in Appendix A to predict steady-state behavior and small signal frequency-response. These predicted results are compared with experimental results.

3.1 Steady-state behavior and ripple

Calculation of steady-state operating point in electronic circuits is fundamental to the subsequent small signal analysis of such circuits for controller design and performance. For switched power electronic circuits, the transient simulation to steady-state often requires brute force simulation over large number of cycles. A number of numerical methods are available to accelerate and solve the general steady-state problem [12], [13], [14] for switched networks. A comparison of some of the time-domain methods for steady-state computations in general power electronic switching circuits is available in [15] where it is shown that the Newton-Raphson algorithm with analytical Jacobian performs better

20

than a large class of algorithms on various examples.

3.1.1 Continuous inductor current mode

For continuous inductor current mode, the calculation of the state variables at the start of a switching cycle, in the steady-state, for the standalone boost converter is a non-iterative algebraic computation.

From Section 2.2.1, combining (2.14) and (2.15), the discrete representation of the boost converter operating in continuous-conduction mode ($\phi_k \geq (1 - d_k)T_s$, $F_3 = I$) at intervals of switching period is obtained as,

$$x_{(k+1)T_s} = F_2 F_1 x_{kT_s} + F_2 G_1 + G_2 \qquad (3.1)$$

where

$$F_1 = e^{A(1)dT_s} \; ; \qquad G_1 = (F_1 - I)A(1)^{-1}B(1)$$
$$F_2 = e^{A(0)(1-d)T_s} \; ; \qquad G_2 = (F_2 - I)A(0)^{-1}B(0)$$

Since in steady-state, $x_{(k+1)T_s} = x_{kT_s}$, (3.1) can be written as,

$$x_{kT_s} = F_2 F_1 x_{kT_s} + F_2 G_1 + G_2$$

that gives the periodic steady-state x_{kT_s} (at constant duty cycle d) as below

$$x_{kT_s} = (I - F_2 F_1)^{-1}(F_2 G_1 + G_2) \qquad (3.2)$$

To illustrate the efficiency of this method, the steady state response of a boost converter from the literature [16], [17] is computed by considering the boost converter with ideal elements $L = 100\mu$H, $C = 4.4\mu$F, $V_d = 5$V, $R_{load} = 8\Omega$, $T = 10^{-4}$s, $D = 0.5$. In [17], the steady-state response is computed using an 82 order matrix representation to

21
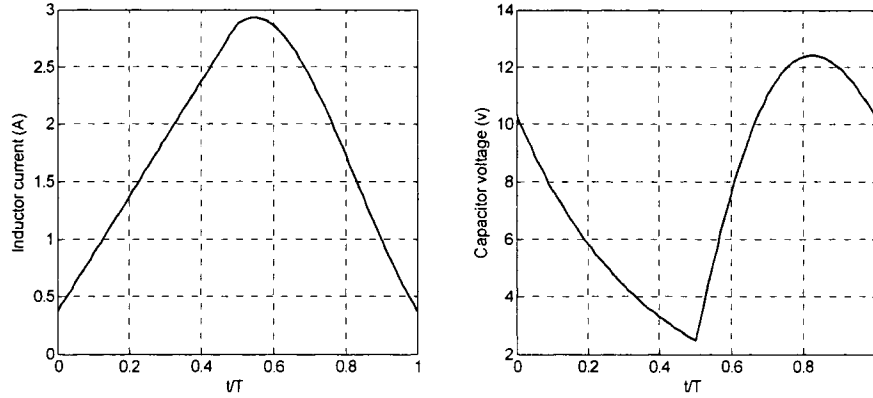
Figure 3-1: Steady-state periodic waveform for boost converter of [17]

obtain the Fourier series coefficients which are then used in the Fourier series expansion to compute the waveform. As opposed to this, the present formulation requires operations with 2×2 matrices to obtain the steady-state boundary values for the state vectors and thereafter the steady-state waveform (ripple) computation with the state-transition matrices (STMs) at fine intervals within the period. The latter operation is effectively carried out using the eigenvector-eigenvalue decomposition of the appropriate $A(S)$ matrices in (2.11). The computed waveforms using the method of this thesis are shown in Fig. 3-1 and are comparable with those reported in the literature cited [16], [17].

3.1.2 Discontinuous inductor current mode

In this subsection, the steady-state behavior of the boost converter in discontinuous-conduction mode is predicted from the discrete-time model and compared with experimental results.

The steady-state discrete representation operating in discontinuous-conduction mode at intervals of the switching period was obtained in (2.27) of Section 2.2.2 as,

$$x_{(k+1)T_s} = F_3 F_2 F_1 x_{kT_s} + F_3 F_2 G_1 + F_3 G_2$$

22

The steady-state vector $x = \begin{bmatrix} 0 & V_C \end{bmatrix}'$ at the beginning of a switching period and (given the steady-state duty cycle D) the unknowns are V_C and ϕ in the steady state. Using the above equation the error vector x_e between final state at the end of one cycle of switching and the state vector x at the beginning of the next switching cycle should be driven to zero for computing V_C and ϕ:

$$x_e = F_3(D,\phi)F_2(\phi)F_1(D)\begin{bmatrix} 0 \\ V_C \end{bmatrix} + F_3(D,\phi)F_2(\phi)G_1(D) + F_3(D,\phi)G_2(\phi) - \begin{bmatrix} 0 \\ V_C \end{bmatrix} \rightarrow \begin{bmatrix} 0 \\ 0 \end{bmatrix}$$
$$(3.3)$$

In the literature, a scalar Newton-Raphson approach with perturbation only on V_C is considered with another scalar Newton-Raphson iteration (or by simulation) for each V_C, for determining ϕ and then the relationship between ϕ and V_C is used implicitly to compute the relevant Jacobian to obtain the steady-state V_C, [14], [15], [18]. For the present problem, in this work, a multivariate Newton-Raphson type numerical approach using two perturbations variable ϕ, V_C is used to drive the 2×1 error vector x_e to zero. Since the necessary Jacobian (2.35) can be worked out analytically, this is observed to be efficient in simultaneously computing ϕ and V_C for the steady state.

The procedure, shown as a flowchart in Fig. 3-2 for solving (3.3), is begun with first computing the inductor current (state variable) from the continuous-conduction mode using (3.2). If it is negative, then the capacitor voltage also obtained from (3.2) and switch off time $(1 - D)T_s$ are taken as the initial values for V_C and ϕ respectively for the Newton-Raphson numerical iterations for computing the steady-state in discontinuous-conduction mode. For analytical purpose, the two columns of the 2×2 Jacobian of (3.3) are derived as,

$$J = \begin{bmatrix} \frac{\partial x_e}{\partial \phi} & \frac{\partial x_e}{\partial V_C} \end{bmatrix}$$

$$\frac{\partial x_e}{\partial \phi} = \begin{bmatrix} 0 & 0 \\ 0 & -a_{22}e^{a_{22}((1-D)T_s - \phi)} \end{bmatrix}\begin{bmatrix} F_2F_1\begin{bmatrix} 0 \\ V_C \end{bmatrix} + F_2G_1 + G_2 \end{bmatrix} \qquad (3.4)$$

23
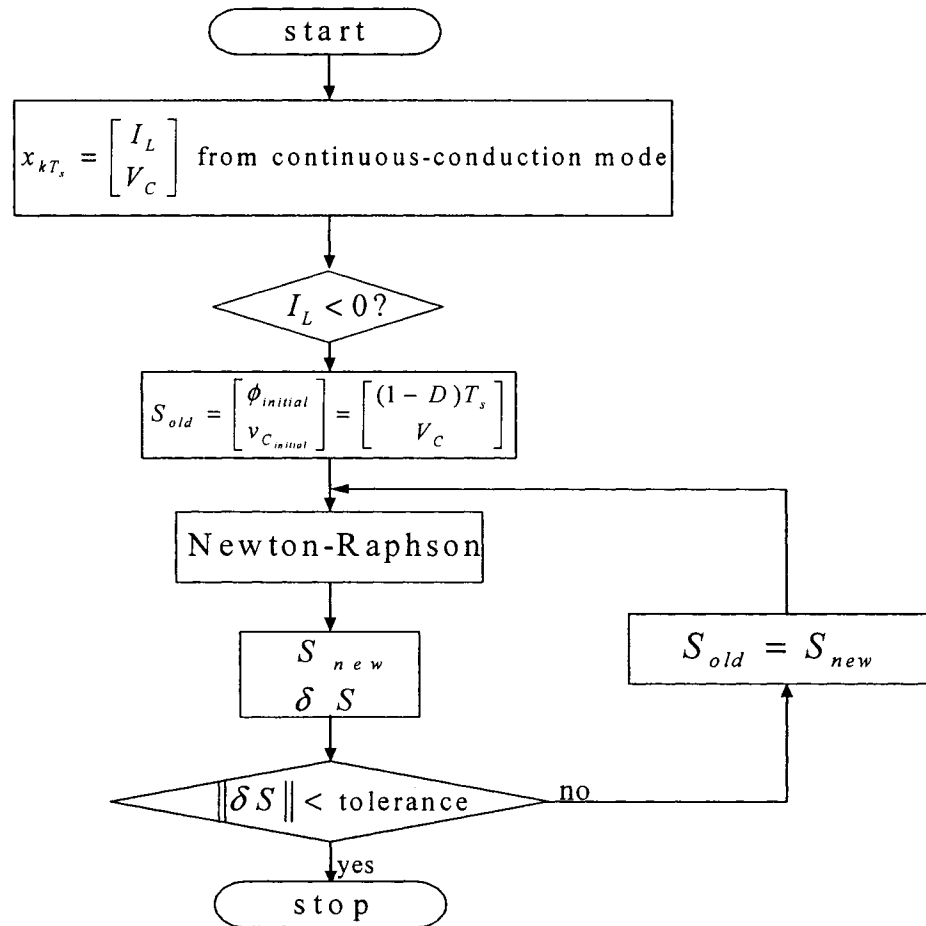
Figure 3-2: Newton-Raphson technique to compute steady-state operating point

24

$$+F_3 \left[A(0)F_2F_1 \begin{bmatrix} 0 \\ V_C \end{bmatrix} + A(0)F_2G_1 + F_2B \right]$$

$$\frac{\partial x_e}{\partial V_C} = [F_3F_2F_1 - 1] \begin{bmatrix} 0 \\ 1 \end{bmatrix}$$

Once the steady-state boundary condition state vector x is determined, then the state variables in between switching periods can be computed using the discrete-time model with small time step. Thus, the discrete-time model can predict the average of state variables at steady-state as well as the ripple waveform within a switching period. As an example, for a boost converter with parameters given in Appendix A, the state variables in between switching periods are computed by discretizing (2.10) during the switch on time and during switch off time with small time step (e.g. $h = 0.1$ μs). Considering x as initial condition, the state variables at each time step are calculated. The results of such computation for the boost converter with $V_0 = 18.8$V, $I_L = 0.52$A and $D = 0.4$ are shown in Fig. 3-3.(a).

In steady-state, ϕ and V_C are calculated as $0.3786T_s$ and 18.7990V respectively. The iterations converge with a 2-norm tolerance on δS in Fig. 3-2 of ϵ in 6 iterations, where ϵ is the default MATLAB floating point relative accuracy. For tolerance below this value, numerical improvement in convergence is not achieved in the current MATLAB implementation. It is noticed that the non-ideal components (r_F, V_F, r_{DS}) involved affecting the tolerance setting.

For the boost converter experimental setup, Fig. 3-3.(b) shows the ripple at inductor current and output voltage respectively. The ripple in those waveforms is obtained in open-loop situation with the nominal operating point $D = 0.4$, $V_0 = 18.8$V, and $I_L = 0.52$A with the boost converter system working in discontinuous-conduction mode. Although the spike induced by MOSFET turn-off/Diode turn-on was shown at the ripple of the experimental output voltage waveform, the linear interpolation of the output voltage trend backwards to switching point matches with the simulation results. The

25
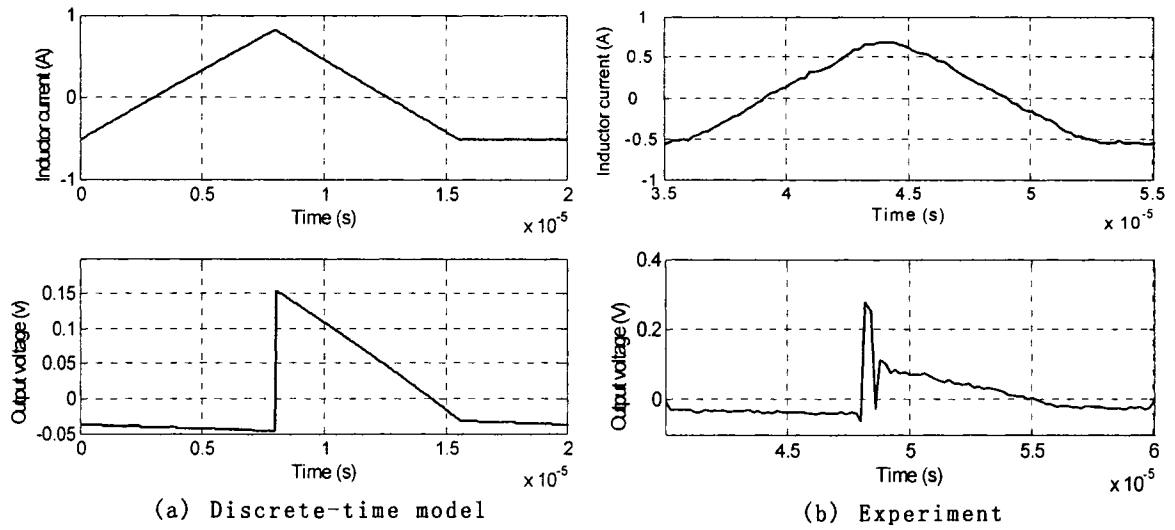
Figure 3-3: Steady-state ripple with DC bias removed for discrete-time model and experiment

experimental current waveform in Fig. 3-3.(b) is captured by using a current probe. The accuracy of this probe is related to its allowable bandwidth (100kHz) and current peak. So for this experiment with a switching frequency (f_s = 50kHz), since only a limited number of harmonics (2) enter into the display, the error between the simulated and experimental ripple in the waveforms shown in the Fig. 3-3 is inevitable and reasonable.

It is to be noted that the discrete-time model accurately predicts these waveforms as shown in Fig. 3-3.

3.2 C-code based simulation and experimental frequency-response

In this section, the frequency-response of the boost converter in discontinuous-conduction mode is obtained experimentally and compared with the frequency-response from C-code based simulation. This is done to estimate the equivalent series resistance (ESR) of the

26
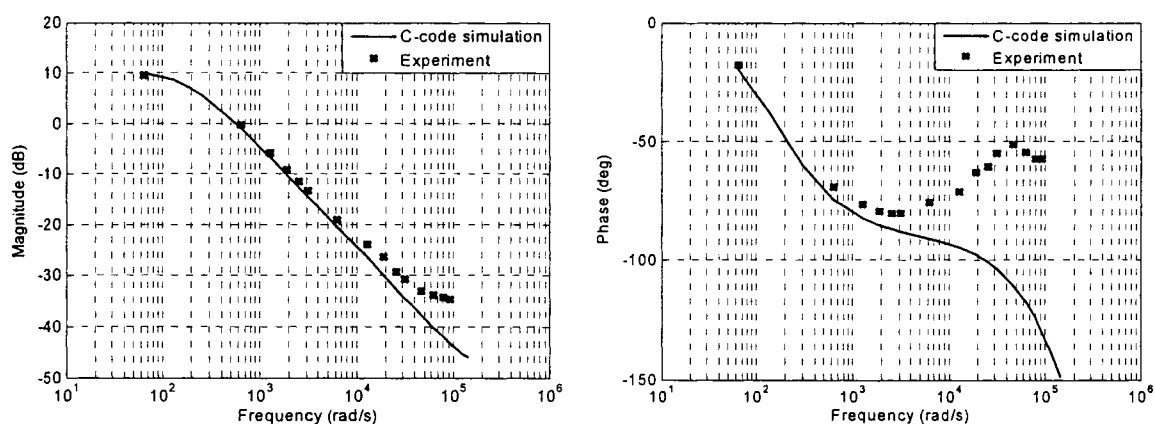
Figure 3-4: Magnitude and phase frequency-responses with $r_c = 0$

capacitor in the boost converter.

The frequency-response of C-code based simulation model is obtained with a input control signal $v_{control}$, given in (3.5), which consists of a DC bias voltage V_{dc} plus a sinusoidal variation of amplitude A and frequency f. The DC voltage is chosen to provide the desired output voltage and keep the converter working at the desired operating point. The amplitude of the sinusoidal signal is $A = 0.1V$ while its frequency f varies over a certain range.

$$v_{control} = V_{dc} + A\sin(2\pi f t) \qquad f = 10\text{Hz to } 25\text{kHz} \qquad (3.5)$$

For the study of small-signal behavior it naturally requires small variations of input duty cycle around a steady-state operating point. The sinusoidal variation of amplitude $A = 0.1V$ corresponds to a variation of ± 0.01 in duty cycle and this variation on duty cycle is quite small (variation of 2.5%), compared to the operating duty cycle of 0.4.

Fig. 3-4 shows the comparison between the experimental system frequency-response and that obtained from C-code based simulation with parameters given in Appendix A but with $r_c = 0$. It clearly shows that the magnitude and phase frequency-responses do not match well.

27
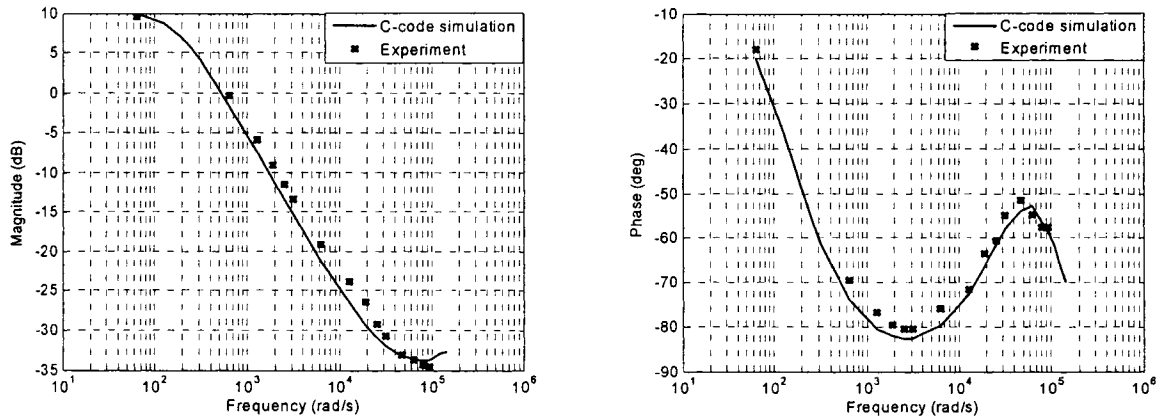
Figure 3-5: Magnitude and phase frequency-responses with $r_c = 0.15\Omega$

3.2.1 Equivalent series resistance (ESR) of capacitor

With C-code based simulation model, the values of all variables have been chosen equal to the component values of the experimental setup. As far as all non-ideal elements, the equivalent values are selected within the range specified for components in the datasheet. The reason for variance in the frequency-response shown in the foregoing section, might be due to the ESR of the capacitor, denoted by r_c in Section 2.1, for which no data is available in the datasheet. In the real system r_c exists, but it is not easily measurable. Fig. 3-4 shows C-code based simulation result without considering the effect of r_c compared to the experimental result. Obviously, the mismatch is clear. Thereafter, using C-code based simulation model, with different values of r_c, the different frequency-responses are obtained and compared with the experimental frequency-response. It was found that for a certain value of r_c, the simulation result matches the experimental result and this corresponding value is chosen as the ESR of the capacitor. The frequency-response obtained from C-code based simulation considering $r_c = 0.15\Omega$ and compared with the experimental frequency-response is illustrated in Fig. 3-5.

The good fit is evident and this value of r_c is used as the ESR of the capacitor. This

28

value was also used in Section 3.1 in the steady-state computation.

3.3 Frequency-response of the discrete-time model

In this section, the frequency-response obtained from the new discrete-time model in Section 2.2 with the input signal v_{in} given in (3.6) with an amplitude of sine-wave $A = 0.1V$, is compared with the frequency-response of C-code based simulation model with a input control signal $v_{control}$ given in (3.5) and the amplitude of sine-wave $A = 0.1V$.

$$v_{in} = V_{dc} + A\sin(2k\pi fT_s) \qquad f = 10\text{Hz to } 25\text{kHz} \qquad (3.6)$$

With (3.6) and (1.1), the duty cycle is written as,

$$d_k = d_o + d_1 \sin(2k\pi fT_s) \qquad (3.7)$$

where

$$d_k = \frac{v_{in}}{\widehat{V}_{st}}, \; d_o = \frac{V_{dc}}{\widehat{V}_{st}} \text{ and } d_1 = \frac{A}{\widehat{V}_{st}}$$

The amplitude of 0.1V corresponds to an amplitude of $d_1 = 0.01$ for $\widehat{V}_{st} = 10V$. As Fig. 3-6 shows, C-code based simulation and the discrete-time model based frequency-response do not match well especially at high frequencies in the phase response. The frequency-response obtained from C-code based simulation is a continuous frequency-response while the other one obtained from the discrete-time model is a discrete frequency-response. The errors between these two are obvious and it is observed that significant part of the errors is due to the ZOH assumption in the discrete time and this is next compensated.

The switching frequency f_s of the discrete-time model can be considered as the sampling rate, and by the *Nyquist Sampling Theorem* the discrete frequency-response from this new model is valid up to a maximum frequency $\frac{f_s}{2}$ Hz or $\frac{\pi}{T_s}$ rad/s [19].

For the boost converter example in this thesis, the sampling rate for the discrete-time

29
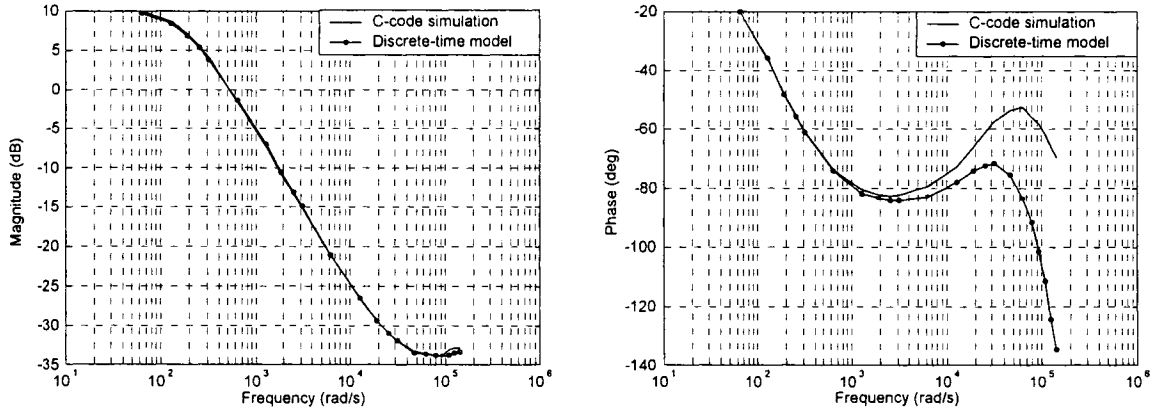
Figure 3-6: Magnitude and phase of frequency-responses

model (switching frequency f_s) is

$$f_s = 50\text{kHz}$$

The corresponding highest frequency f_h, for which the frequency-response is valid,

$$f_h = \frac{f_s}{2} = 25\text{kHz} \qquad (25\text{k} \times 2\pi \simeq 2 \times 10^5 \text{ rad/sec})$$

Although the frequency-responses shown in Fig. 3-6 are plotted within the range of the highest frequency (between 10Hz and 25kHz), the discrepancy at higher frequencies in phase shift of the frequency-response can be seen.

3.4 Zero-order hold

Zero-order hold (ZOH) is one of methods to generate a continuous input signal $f(t)$ by holding each sample value $f[kT]$ constant over one sample period, where T is sampling time and k is sampling number. Zero-order hold accepts a sample $f[kT]$ at $t = kT$ and holds it until the next sample $f[(k+1)T]$ arrives at $t = kT+T$. In developing the discrete-time model, the conversion from continuous-time to discrete-time is done assuming zero-

30

order hold on duty cycle. In the frequency-response computation, the sine-wave input in the discrete-time frequency-response is a stepped staircase like sinusoidal waveform and then introduces some error between the two frequency-responses. So, the effect of the zero-order hold on this discrete frequency-response is studied in this section.

3.4.1 Transfer function of the zero-order hold

In time-domain, a zero-order hold can be given by the following piecewise function,

$$f_k(t) = f[kT] \qquad kT \le t < (k+1)T$$

The impulse response $h(t)$ of the zero-order hold is expressed as,

$$h(t) = u(t) - u(t - T) \tag{3.8}$$

where $u(t)$ is unit-step function. In (3.8), taking Laplace transform, the transfer function is given by

$$H(s) = \frac{1}{s} - \frac{e^{-sT}}{s} \tag{3.9}$$

In (3.9), substituting jw for s, the frequency-response of ZOH can be obtained as,

$$H(jw) = \frac{1}{jw} - \frac{e^{-jwT}}{jw} = T\frac{e^{-\frac{iwT}{2}}(e^{\frac{iwT}{2}} - e^{-\frac{iwT}{2}})}{2j\frac{wT}{2}} = T\frac{\sin(\frac{wT}{2})}{\frac{wT}{2}}e^{-\frac{iwT}{2}} \tag{3.10}$$

3.4.2 Frequency-response of the sampled signal

In order to compensate the frequency-response of the discretized model, the continuous transfer function of the zero-order hold is not sufficient. A sampled version of the zero-order hold should be derived. In this subsection, the relation between the frequency-response of a continuous signal and the frequency-response of a sampled signal is obtained as per [19].

A continuous signal $f(t)$ is converted into a train of narrow pulses $f^*(t)$ which repre-

31

sents a discrete signal resulting from sampling occurring at the sampling instances 0, T, $2T, \cdots, kT, \cdots$, given by,

$$f^*(t) = f(t)\delta_T(t) = f(t) \sum_{k=-\infty}^{\infty} \delta(t - kT) \tag{3.11}$$

Since the impulse train $\delta_T(t)$ is periodic, it can be expanded in a complex Fourier series.

$$\delta_T(t) = \frac{1}{T} \sum_{n=-\infty}^{\infty} e^{jnw_s t} \tag{3.12}$$

where $w_s = \frac{2\pi}{T}$. Combining (3.11) and (3.12) gives

$$f^*(t) = \frac{1}{T} \sum_{n=-\infty}^{\infty} f(t) e^{jnw_s t} \tag{3.13}$$

Taking Laplace transformation of (3.13) and substituting jw for s, the frequency-response of $f^*(t)$ is given by,

$$F^*(jw) = \frac{1}{T} \sum_{n=-\infty}^{\infty} F[\, j(w + nw_s)\,] \tag{3.14}$$

By passing $F^*(\,jw\,)$ through an ideal lowpass filter $H(jw)$ given by,

$$H(jw) = \{ \begin{array}{ll} 1, & |w| \leq w_s \, / \, 2 \\ 0, & |w| > w_s \, / \, 2 \end{array}$$

The base band frequency-response characteristics are obtained in the absence of aliasing as,

$$F^*(\,jw\,) = \frac{1}{T} F(\,jw\,) \tag{3.15}$$

which is the same as (3.14) with $n = 0$.

(3.15) shows the relation between the frequency-response of a continuous signal $F(jw)$ and the frequency-response of a sampled signal $F^*(jw)$ in the base band.

32

3.4.3 Zero-order hold compensation

(3.10) represents the continuous frequency-response of the zero-order hold. When combined with (3.15), the frequency-response of the sampled zero-order hold signal in absence of aliasing is given by:

$$H^*_{ZOH}(jw) = \frac{1}{T}H(jw) = \frac{\sin(\frac{wT}{2})}{\frac{wT}{2}}e^{-\frac{jwT}{2}} \tag{3.16}$$

in this base band.

It can be seen that if the sampling period T is very small the zero-order hold amplitude will be very close to '1' and its phase will be very close to '0'. In other words the zero-order hold will have almost no effect on the frequency-response of the discretized system. But for bigger values of the sampling period T, the zero-order hold will have some noticeable magnitude and phase change that will affect the frequency-response of the discretized system. From (3.16) the change introduced by zero-order hold in the frequency-response of the discretized system is more apparent at higher frequencies.

3.5 ZOH compensated frequency-response of the discrete time model

If the discrete-time frequency-response obtained in Section 3.3 is denoted by $G_d(e^{jwT_s},$ $d_o, d_1)$, using (3.16), the ZOH compensated continuous-time frequency-response $G(jw,$ $d_o, d_1)$ is given by,

$$G(jw, \ d_o, \ d_1) = G_d(e^{jwT_s}, \ d_o, \ d_1)\frac{wT_s/2}{\sin(wT_s/2)}e^{jwT_s/2} \tag{3.17}$$

Fig. 3-7 shows the ZOH compensated magnitude and phase plots of the frequency-responses of the discrete-time model compared with the C-code based results respectively. These results compared to Fig. 3-6 clearly show that the ZOH compensation does improve

33
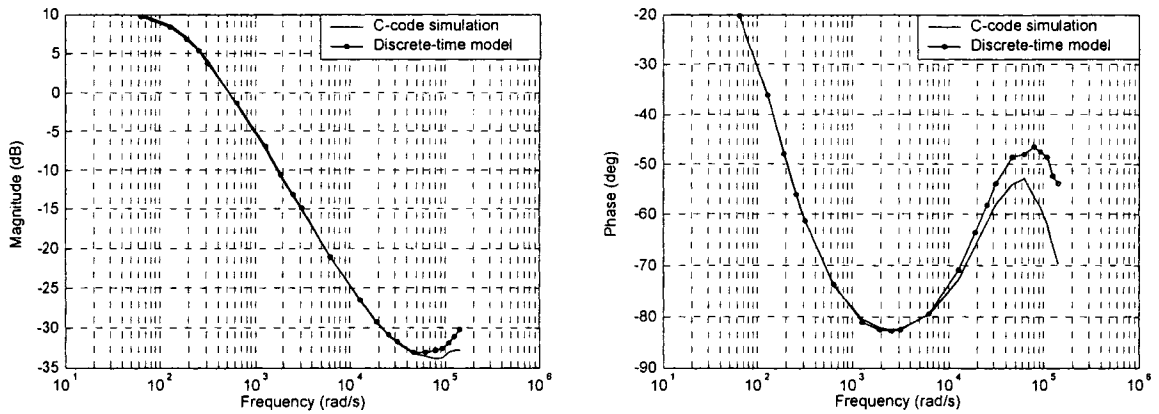
Figure 3-7: Compensated magnitude and phase of frequency-responses

the frequency-response of the discrete-time model significantly.

It is also noticed that even after compensation there are still some error at higher frequencies on magnitude and phase responses. Due to aliasing, this problem will be reduced if higher switching frequencies (i.e. smaller switching periods) are used for the PWM in the boost converter. While the switching frequency of the experimental setup of the boost converter in this thesis is $f_s = 50\text{kHz}$, in practice boost converters are usually designed for higher switching frequencies. For instance, when the boost converter is designed for a higher switching frequency $f_s = 400\text{kHz}$, Figs. 3-8 and 3-9 illustrate the magnitude and phase frequency-responses of the discrete-time model before ZOH compensation as well as after ZOH compensation compared with C-code based simulation respectively within the same frequency band. Since the operation mode of the system is at a different higher switching frequency, the boost converter no longer stays in discontinuous inductor current mode. Note that with this higher switching frequency $f_s = 400\text{kHz}$, the error between the frequency-response obtained even before ZOH compensation and that obtained from C-code based simulation is reduced significantly. The zero-order hold has only slight effect on the frequency-response of the discretized system at high switching rates.

34
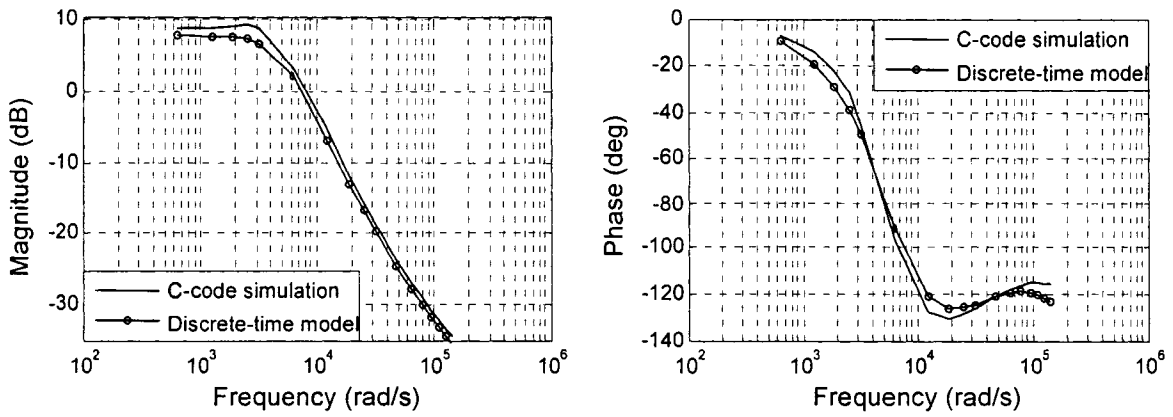
Figure 3-8: Magnitude and phase of frequency-responses before ZOH compensation with $f_s = 400\text{kHz}$
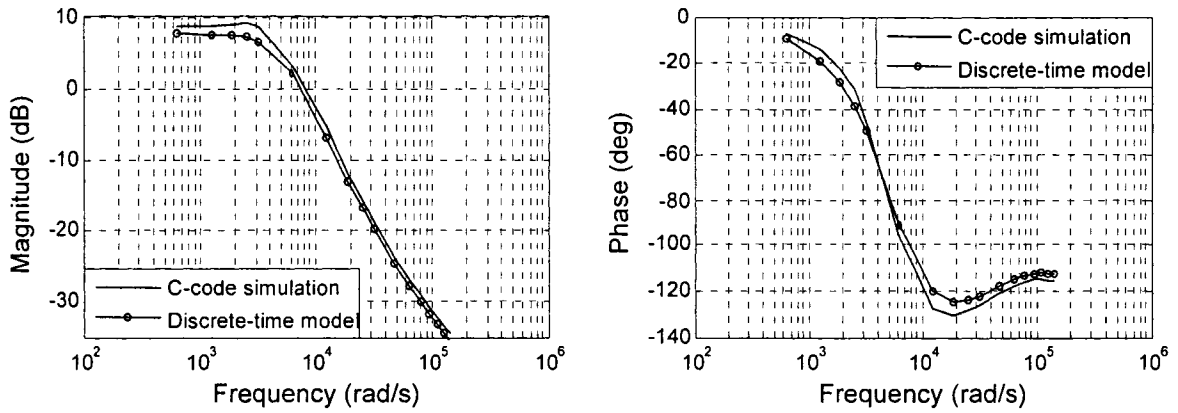
Figure 3-9: Magnitude and phase of frequency-responses after ZOH compensation with $f_s = 400\text{kHz}$

35
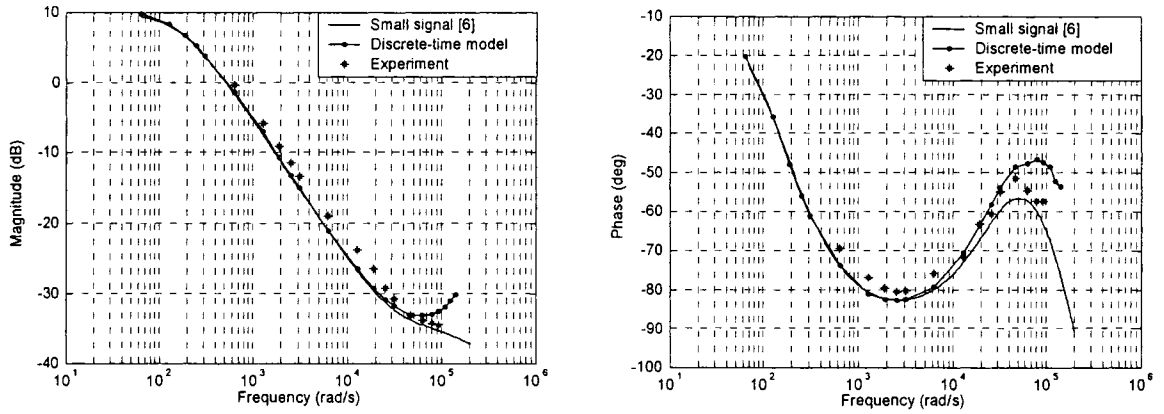
Figure 3-10: Magnitude and phase of small signal frequency-response for discrete-time model and experiment

3.6 Small signal behavior of the boost converter

The models of the boost converter for discontinuous-conduction mode in the literature fall into two categories: the first-order model [4] and second-order models [5], [6]. The first-order model can correctly predict the behavior of a converter in a low-frequency range, resulting in large approximations in the phase response. The second-order models result in a better approximation of the circuit frequency-response. However, some large discrepancies still exist at high frequencies [5].

Since a small-signal circuit model of the boost converter has been derived [6], the small signal frequency-response is obtainable from the expression for the control-to-output transfer function, given in (3.18), derived using the model in [6] in combination with the parameters in Appendix A.

$$G(s) = \frac{-2.256s^2 + 5.631 \times 10^5 s + 2.902 \times 10^9}{s^2 + 3.584 \times 10^5 s + 1.775 \times 10^8} \tag{3.18}$$

In the light of this comparison shown in Fig. 3-10, the frequency-response obtained from the discrete-time model predicts the small signal behavior of the boost converter in

36

discontinuous-conduction mode of operation and yields same conclusions as in [5], and [6]. It is shown that this newly developed discrete-time model of this thesis is able to predict the small signal frequency-response.

3.7 Newton-Raphson technique to accelerate the computation speed of the frequency-response

Thus far, the small signal frequency-response of the boost converter operating in discontinuous inductor current mode has been obtained with the discrete-time model. Even though the computation of the frequency-response using the discrete-time model takes less time than using C-code based simulation with very fine time-steps, it is still a time-consuming process. Since the frequency-response of the discrete-time model at any frequency is achieved by comparing the magnitude at that frequency in the output voltage and its phase shift with input sinusoid, the overall frequency-response needs be done at each frequency. Therefore, an alternative faster method using Newton-Raphson technique to accelerate the computation of the frequency-response from the developed discrete-time model is introduced here. Note that the Newton-Raphson technique applied in this section is discussed briefly in Sections 2.2.4 and 3.1. For discontinuous-conduction mode, computing the periodic steady-state vector starts with state vector $x_{kT_s} = \begin{bmatrix} 0 & V_C \end{bmatrix}'$ at each switching period (T_s) and the input sinusoidal waveform value (d_k), then the state vector $x_{(k+1)T_s}$ at the beginning of the next switching period is computed after computing the corresponding ϕ_k as discussed in Section 2.2.4. The procedure is repeated up to $x_{(k+N)T_s}$ where N is the integer ratio between the frequency at which the response is desired and switching frequency. Newton-Raphson technique with numerical Jacobian computation is needed to make the error $(x_{(k+N)T_s} - x_{kT_s})$ tend to zero to obtain the periodic steady-state vector. Once the periodic steady-state vector is formed, the intermediate states are computed so that magnitude and phase response is computed at that frequency.

37
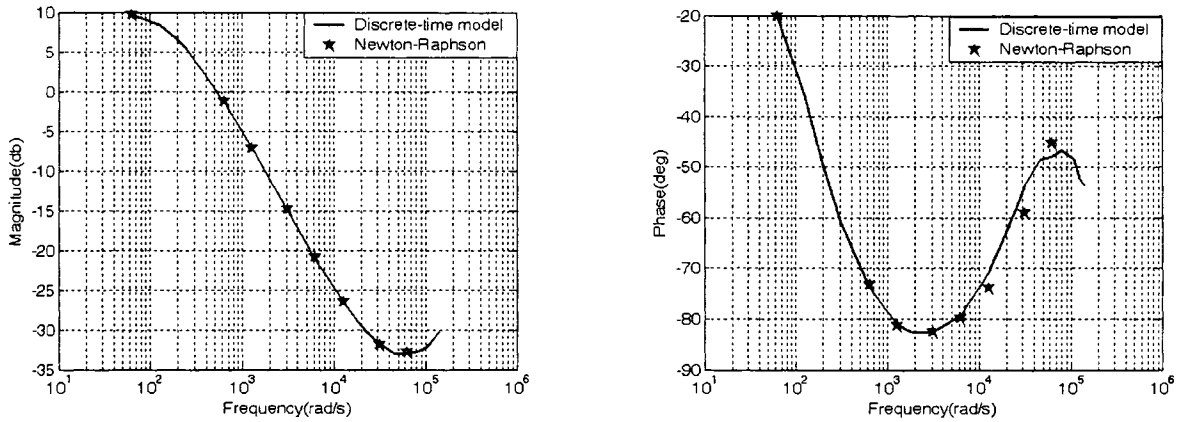
Figure 3-11: Newton-Raphson method to accelerate the computation of the frequency-response

- Only input sine-wave in steady-state at that frequency is used for computing frequency-response of the boost converter at that frequency.

- While in the above writing, it is to be noted that this accelerated technique of computation presupposes that the ratio of the frequency $f = \frac{w}{2\pi}$, at which the response is sought to the switching frequency $f_s = \frac{1}{T_s}$ is an integer, the method can be easily extended to the case when the ratio is one of rational numbers.

Fig. 3-11 shows that the accelerated approach considering one sinusoidal period of steady-state for the magnitude and phase frequency-response is in agreement with that computed from the discrete-time model approach outlined in earlier sections. The comparison of computing time between the previous approach using the discrete-time model and the Newton-Raphson method at seven frequency points at which the response is sought is given in Tables 3-1 and 3-2. For Table 3-2, an initial steady-state vector $x_{initial} = [\ 0 \quad 0\ ]'$ and a *tolerance* value (10^{-7}) is used to detect convergence of the computation to the periodic steady-state vector. From the Tables, it is evident that the Newton-Raphson technique does accelerate the computation speed of the frequency-response, over the direct approach in the discrete-time model by almost six times within

38

the specific frequency range (100Hz ~ 10kHz).

Table 3-1 Direct frequency-response from the discrete-time model

Frequency(Hz) f	100	200	500	1000	2000	5000	10000
Time (Sec)	39.8	39.8	39.8	39.9	40.1	40.1	40.1
Cumulative time (Sec)	279.6						

Table 3-2 Newton-Raphson method of computing the frequency-response

$$f_s = 50 \text{ kHz} \; ; \; x_{initial} = [\; 0 \quad 0 \;]' ; \; tolerance = 10^{-7}$$

Frequency(Hz) f	100	200	500	1000	2000	5000	10000
Sampling points $N = \frac{f_s}{f}$	500	250	100	50	25	10	5
Iterations	5	11	27	55	110	275	550
Time (Sec)	13.5	8.8	5.7	4.8	4.2	4	3.9
Cumulative time (Sec)	44.9						

Increasing the *tolerance* value, it was found that larger tolerance value requires less iterations (a *tolerance* of 10^{-3} leads to results in Table 3-3). Once the DC steady-state operating point $x_{initial} = [\; 0 \quad 18.8 \;]'$ is taken as the initial value of the periodic steady-state vector at each frequency, both iterations and computation speed of convergence can be reduced significantly even with a small *tolerance* value (10^{-9}) as shown in Table 3-4. Note that the selection of the initial value of the steady-state vector evidently affects the iterations of convergence to compute the frequency-response using the Newton-Raphson approach.

Table 3-3 Newton-Raphson method of computing the frequency-response

$$f_s = 50 \text{ kHz} \; ; \; x_{initial} = [\; 0 \quad 0 \;]' ; \quad tolerance = 10^{-3}$$

Frequency(Hz) f	100	200	500	1000	2000	5000	10000
Sampling points $N = \frac{f_s}{f}$	500	250	100	50	25	10	5
Iterations	3	5	14	28	55	139	279
Time (Sec)	13	7.1	4.5	3.5	3.1	2.8	2.78
Cumulative time (Sec)	36.8						

39

Table 3-4   Newton-Raphson method of computing the frequency-response

$$f_s = 50 \text{ kHz} \; ; \; x_{initial} = [\; 0 \quad 18.8 \;]' ; \; tolerance = 10^{-9}$$

Frequency(Hz) f	100	200	500	1000	2000	5000	10000
Sampling points $N = \frac{f_s}{f}$	500	250	100	50	25	10	5
Iterations	1	2	4	4	3	0	0
Time (Sec)	10.7	5.7	2.6	1.33	0.64	0.24	0.18
Cumulative time (Sec)	21.39						

3.8   Conclusion

The calculation of steady-state operating point and ripple in PWM DC-DC boost converters using the discrete-time model of Chapter 2 which involves at most 2×2 matrices and Newton-Raphson iterations is considered in this chapter. Analytical expressions for the Jacobian's needed in the Newton-Raphson iterations have been developed and used. This discrete-time model accurately predicts the steady-state and small signal behavior when compared with experimental results and published literature.

The study on steady-state behavior and small signal frequency-response considers the values of the non-ideal component parameters r_c, r_L, r_{DS}, r_F, and V_F in simulations, as their effect on the boost converter behavior in this experimental system is rather significant.

The small signal frequency-response obtained from the discrete-time model verifies the same results as those given by [6] for discontinuous-conduction mode. Compensation for ZOH is necessary, due to low switching rate used in this work, especially for phase response. This newly developed discrete-time model however can provide large signal frequency-response with respect to large variations on input control signal $v_{control}$ along the line of [9] and compute the response in both continuous and discontinuous modes. Due to the relatively big ripple in the presence of exclusively discontinuous inductor current mode, it is difficult to experimentally measure the large signal frequency-response in the

40

experimental setup.

The use of the Newton-Raphson technique to accelerate the computation of the frequency-response from the developed discrete-time model has also been studied and shown to be superior in computational efficiency compared with direct computation of the response from the discrete-time model.

41

Chapter 4

Closed-loop behavior analysis

In Chapter 3, the focus of this work was mostly on the steady-state behavior of the standalone (open-loop) boost converter, which comprises steady-state and ripple as well as small signal frequency-response. In analyzing a control system, referring to Fig. 1-2 the transient response of the system to specific test input signals is indispensable. In this Chapter, the models discussed in Chapter 2 are used to compute the output transient behavior in the case of closed-loop control system using output proportional and integral (PI) feedback. The circuit diagram of the experimental setup and the details of the circuit are given in Appendix B.

4.1   C-code based simulation and experimental closed-loop output-response

In this section, the closed-loop output-response of the boost converter for a particular setting of PI control ($K_p = 0.4$; $K_i = 1000$ per sec in the experimental setup of Appendix B) is obtained experimentally and compared with the closed-loop output-response from C-code based simulation.

In this control system (Appendix B), the actuating error signal, which is the difference between the input signal and feedback signal (the output voltage in this circuit), is fed
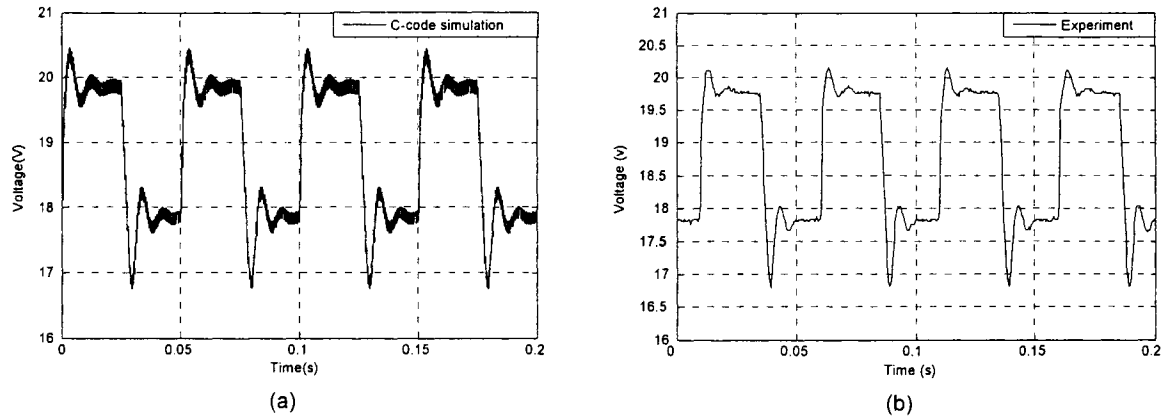
Figure 4-1: Closed-loop output-responses with $B = 1$V. (a) C-code based simulation. (b) Experiment.

to an analog PI controller so as to reduce the error and bring the output voltage of the boost converter to a desired value V_{ref}. For experimental purpose, the input signal V_{ref} of this closed-loop control system is excited by a square-wave signal of amplitude $B = 1$V and frequency $f_1 = 20$Hz superimposed on a nominal value of the DC output feedback voltage level $V_o = 18.8$V, which keeps the system working at the nominal operating point. The frequency f_1 provides the system sufficient time to reach steady-state before the next perturbation in the set-point.

The closed-loop output-response of C-code based simulation model is obtained using the same input excitation. Fig. 4-1 shows the comparison between C-code based simulation and the experimental closed-loop output-response for this boost converter.

Note that since the closed-loop output-response from C-code based simulation is computed with very fine time step (0.005μs) which is far less than switching period (20μs), the output-response shown in the Fig. 4-1.(a) provides instantaneous values of the output voltage. The experimental output-response however refers to the average output voltage captured with a sampling period (0.4ms) in an oscilloscope, which is much bigger than the switching period. This comparison in Fig. 4-1 illustrates that the result computed

43
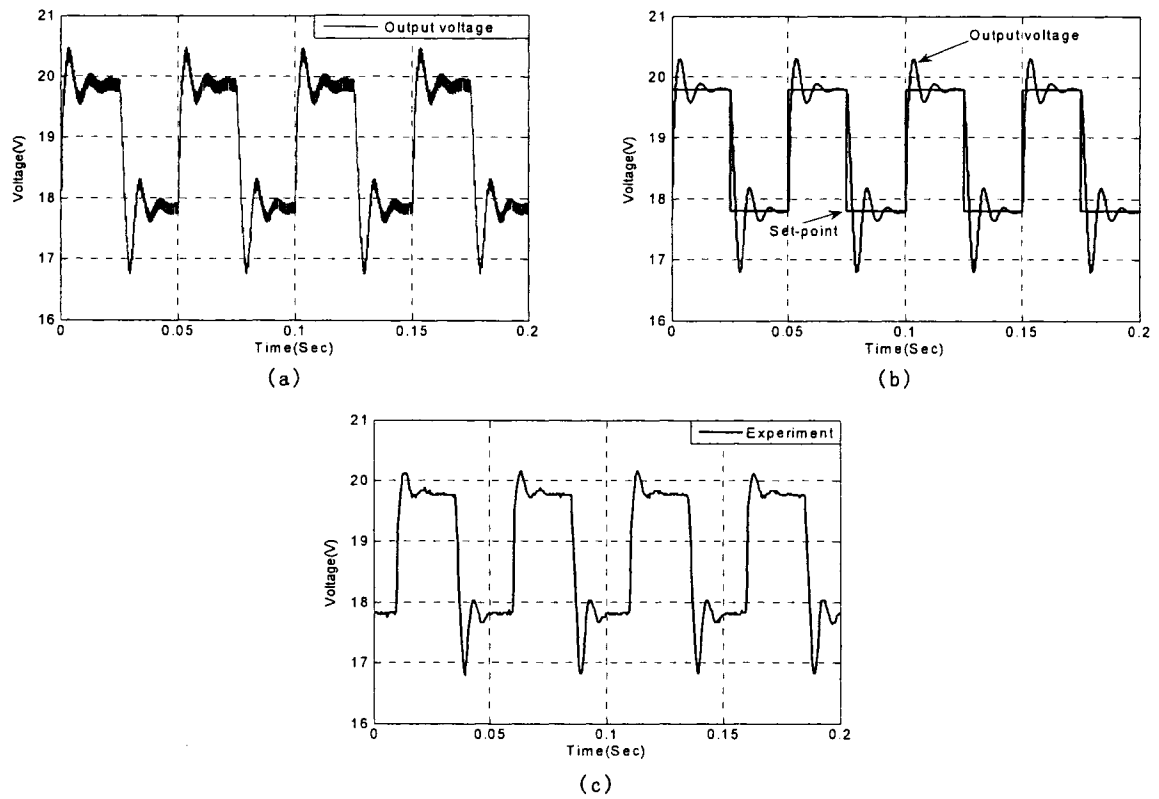
Figure 4-2: Closed-loop output-responses with $B = 1V$. (a) Discrete-time model (instantaneous values of output). (b) Discrete-time model (average values of output). (c) Experiment.

from C-code based simulation model manifests agreement with the experimental result and the output-response tracks the desired set-point changes.

It can be seen that nonlinear (large signal) behavior is present, in that the overshoot on the increasing perturbation is smaller than on the decreasing perturbation in the set-point.

44

4.2 Closed-loop output-response of the discrete-time model

With the same excitation of the previous section, in Fig. 4-2, the closed-loop output-response obtained using the discrete-time model in combination with Newton-Raphson iterations (for ϕ) is compared with the closed-loop output-response of C-code based simulation and experiment. With the quantitative comparison of the percent overshoot and settling time on both increasing and decreasing perturbations of the set-point in Table 4-1, it is evident that the discrete-time model shown in Fig. 4-2, makes good prediction of the experimental and C-code based simulation. It also captures the nonlinear behavior on the increasing and decreasing perturbations.

Table 4-1   Percent overshoot and settling time comparison with nonlinear behavior

Overshoot and settling time on the perturbation	Increasing	Decreasing
Discrete-time model	25%; 20ms	50%; 25ms
Experiment	20%; 15ms	50%; 20ms

4.3 Nonlinear behavior of the boost converter

All closed-loop output-responses so far are obtained with the set-point changes of Section 4.1, which corresponds to a 5% perturbation around operating point voltage of 18.8V. Even though this deviation on input set-point is quite small, Figs. 4-1 and 4-2 illustrate that there is a difference of the response on the upward and downward perturbations of the set-point, indicating that the converter does not behave linearly even for such a small perturbation.

45

4.3.1 Linear behavior

As long as the system operates in discontinuous-conduction mode, no matter what the amplitude of the square waveform is, the response on the upward and downward perturbations of the set-point should be the same (linear behavior). But as soon as the system starts working in continuous and discontinuous modes at some amplitude of the square waveform, the response on the upward and downward perturbations of the set-point excitation will no longer be the same.

To give a numerical example, for the boost converter parameters (Appendix B), the linear model is valid for a perturbation of $|B| \leq 0.201\text{V}$ around DC operating point voltage of 18.8V. This is a region of validity of approximately 1.07% perturbations in the set-point and is quite small.

The discrete-time model which includes both modes of operation predicts the large signal behavior of the converter quite well as seen in Fig. 4-3 where experimental and simulated responses for different amplitudes of the set-point waveform are given. Although not clear from Fig. 4-3, it is interesting to note that for a given B beyond the small signal limit ($|B| > 0.201\text{V}$), the converter closed-loop behavior changes from being entirely in discontinuous-conduction mode (small signal behavior) at small perturbations of amplitude B to behavior with continuous and discontinuous modes (large signal behavior) at larger perturbations of amplitude B. When the amplitude B is at 0.1V, the linear behavior is seen on the response. The presence of continuous and discontinuous inductor current modes in any given closed-loop response for fixed B precludes the use of simpler methods of computation of large signal closed-loop response.

4.3.2 Small signal model

In the literature, in discontinuous-conduction mode, the expression for the small signal transfer function denoted by $G(s)$ given in (3.18) was derived in [6], with the assumption the boost converter is working around a particular discontinuous mode operating point.

46
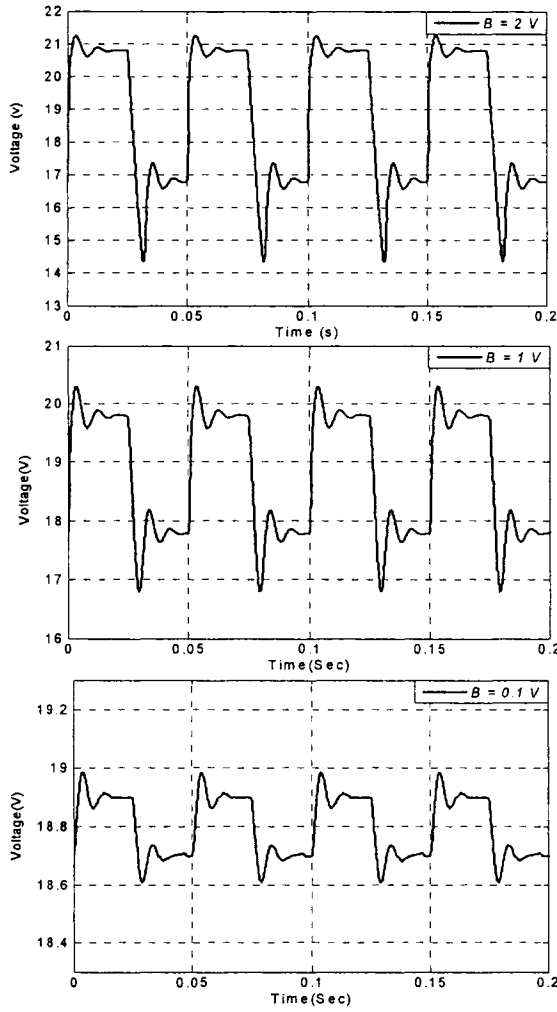
(a) Discrete-time model with different B
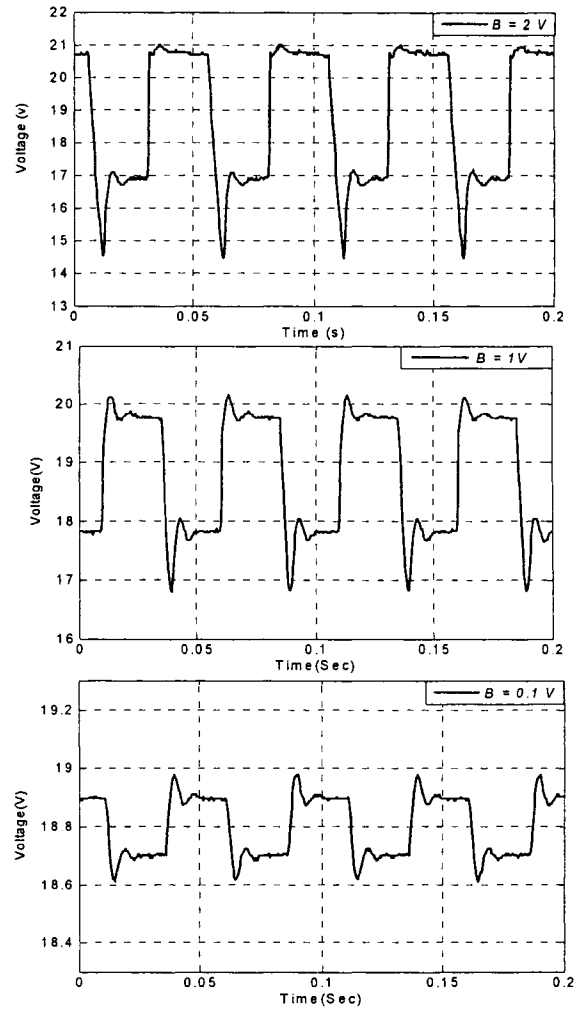
(b) Experiment with different B

Figure 4-3: Closed-loop output-responses for discrete-time model and experiment with different values of B
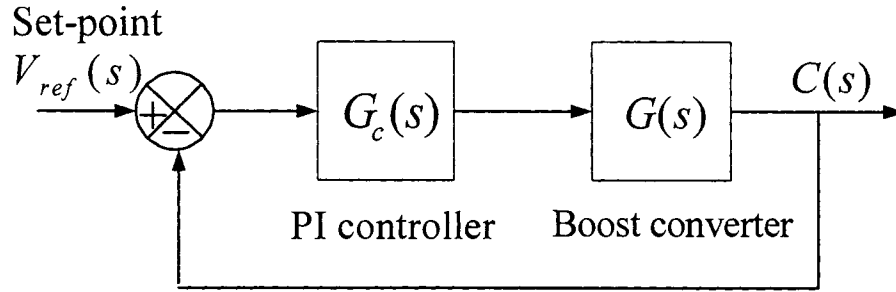
47

Figure 4-4: Control block

Fig. 1-2 can be simplified as the control block shown in Fig. 4-4, then the closed-loop transfer function between the output signal and the input signal is derived as,

$$\frac{C(s)}{V_{ref}(s)} = \frac{G(s)G_c(s)}{1 + G(s)G_c(s)} \tag{4.1}$$

where

$$G_c(s) = k_p + \frac{k_i}{s}$$

which is composed of the proportional gain k_p and the integral gain k_i.

Using (4.1), the unit-step response can be obtained and compared with the small signal closed-loop response obtained from the discrete-time model with $B = 0.1\text{V}$ in Section 4.3.2 as well as the experiment in Fig. 4-5. With the quantitative comparison in Table 4-2, note that even though overshoots on increasing and decreasing perturbations of the set-point computed by the small signal model [6] and the discrete-time model are consistent with the experimental results, the values of the settling time computed from the above two models are not in agreement compared to the experimental results. The discrete-time model exhibits different dynamic characteristic of the settling time on both upward and downward perturbations of the set-point, which is not predicted by small signal model [6]. Thus, this developed discrete-time model predicts better performance characteristics than small signal transfer function in computing closed-loop output-response of the boost converter.
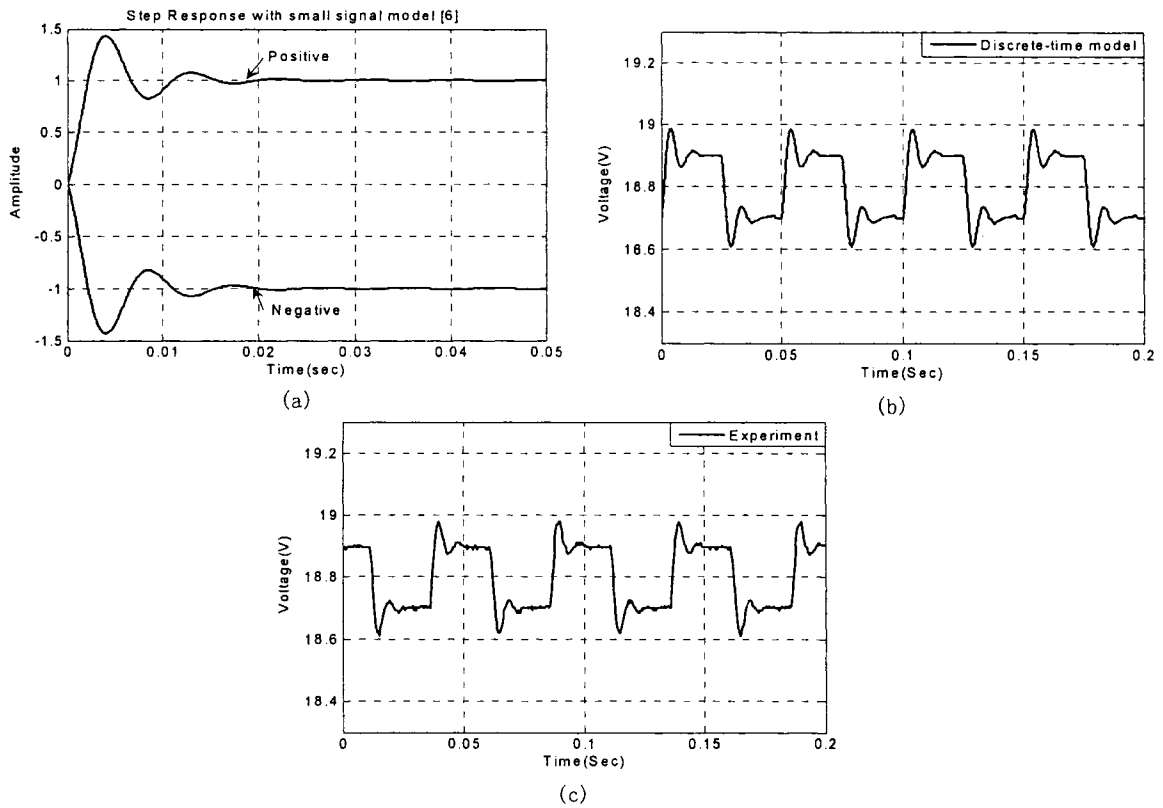
48

Figure 4-5: Closed-loop responses with $B = 0.1\text{V}$ (a) Small signal model [6]. (b) Discrete-time model. (c) Experiment.

49

Table 4-2 Percent overshoot and settling time comparison
with linear behavior

Overshoot and settling time on the perturbation	Increasing	Decreasing
Small signal model in [6]	45%; 23ms	45%; 23ms
Discrete-time model	45%; 14ms	45%; 24ms
Experiment	42%; 13ms	42%; 21ms

4.4 Conclusion

In this chapter, the two models proposed in Chapter 2 are used to compute closed-loop output-response of the boost converter. The small signal model proposed in [6] designed only for discontinuous mode, can not fully predict the system behavior at larger perturbations. Furthermore, while the closed-loop output-response from this small signal model is compared with that obtained from the discrete-time model with amplitude $B = 0.1V$ and experiment, it is found that the discrete-time model can predict it more accurately.

Discrete-time model overcomes the limitation by predicting the behavior in both continuous and discontinuous inductor current modes of operation and predicts the closed-loop behavior of the boost converter better than small signal model of [6].

Chapter 5

Different operating point

All the results presented in the foregoing chapters are obtained for constant value of the load and input line voltage of the boost converter at a nominal operating point. In real power electronic circuits, the consequences of inevitable variations in these parameters cause circuit operation to deviate from the nominal operating point. Any change in the output load or input line voltage affects the output voltages of uncontrolled DC power supplies. With the combination of two different input voltage and two different output loads keeping the converter in discontinuous mode in steady-state with input duty cycle constant, three different operating points under open-loop operation listed in Table 5-1 are considered in this chapter. The operating point $N1$ represents a nominal operating point. The operating points $N2$ and $N3$ refer to the boost converter working in deeper discontinuous inductor current mode with higher inductor current peak.

Table 5-1 Different operating points with constant duty cycle D

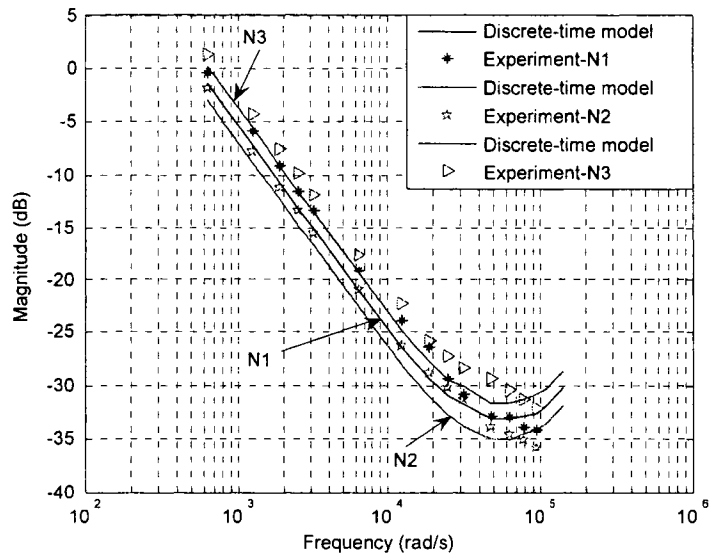| Operating pt	V_d (V)	R_{load} (Ω)	D	V_o (V)(open loop)
$N1$	10	74.94	0.4	18.8
$N2$	10	99.6	0.4	20.7
$N3$	12	74.94	0.4	22.7

51

Figure 5-1: Magnitude response for discrete-time model and experiment with three different operating points.
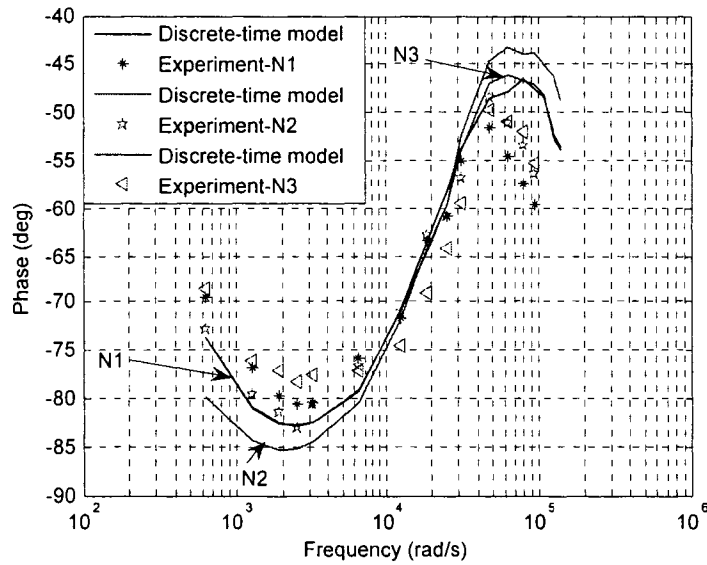

Figure 5-2: Phase response for discrete-time model and experiment with three different operating points.

52

5.1 Small signal frequency-response

As in Chapter 3, the magnitude and phase frequency-responses of open-loop for the three operating points of Table 5-1 between control input and output voltage with input amplitude of sine-wave $A = 0.1$V corresponding to $d_1 = 0.01$ in (3.6) are computed and compared with experimental results in Figs. 5-1 and 5-2 respectively.

The smallness of $d_1 = 0.01$ presents considerable difficulty in measuring the frequency-response from the ripple and noise in the experimental system. Although the variations in the frequency-response are quite small to variations of input line voltage or output load, from Figs. 5-1 and 5-2, it can be seen that this small signal frequency-response of the discrete-time model is dependent on the operating point. The discrete-time model takes into account the operating point and reasonably accurately predicts the small signal frequency-response under different operating points.

5.2 Closed-loop output-response

In this section, under different operating points $N2$ and $N3$, the closed-loop output-responses from the discrete-time model to step set-point changes are obtained and compared with the experimental results. These predicted results shown in Figs. 5-3.(a) and 5-4.(a) correspond with their experimental results shown in Figs. 5-3.(b) and 5-4.(b) respectively. No matter which operating point the boost converter is working at, large signal behavior is exhibited with increasing amplitude of the set-point changes.

Furthermore, it is seen that this discrete-time model predicts the system behavior with and without feedback adequately.
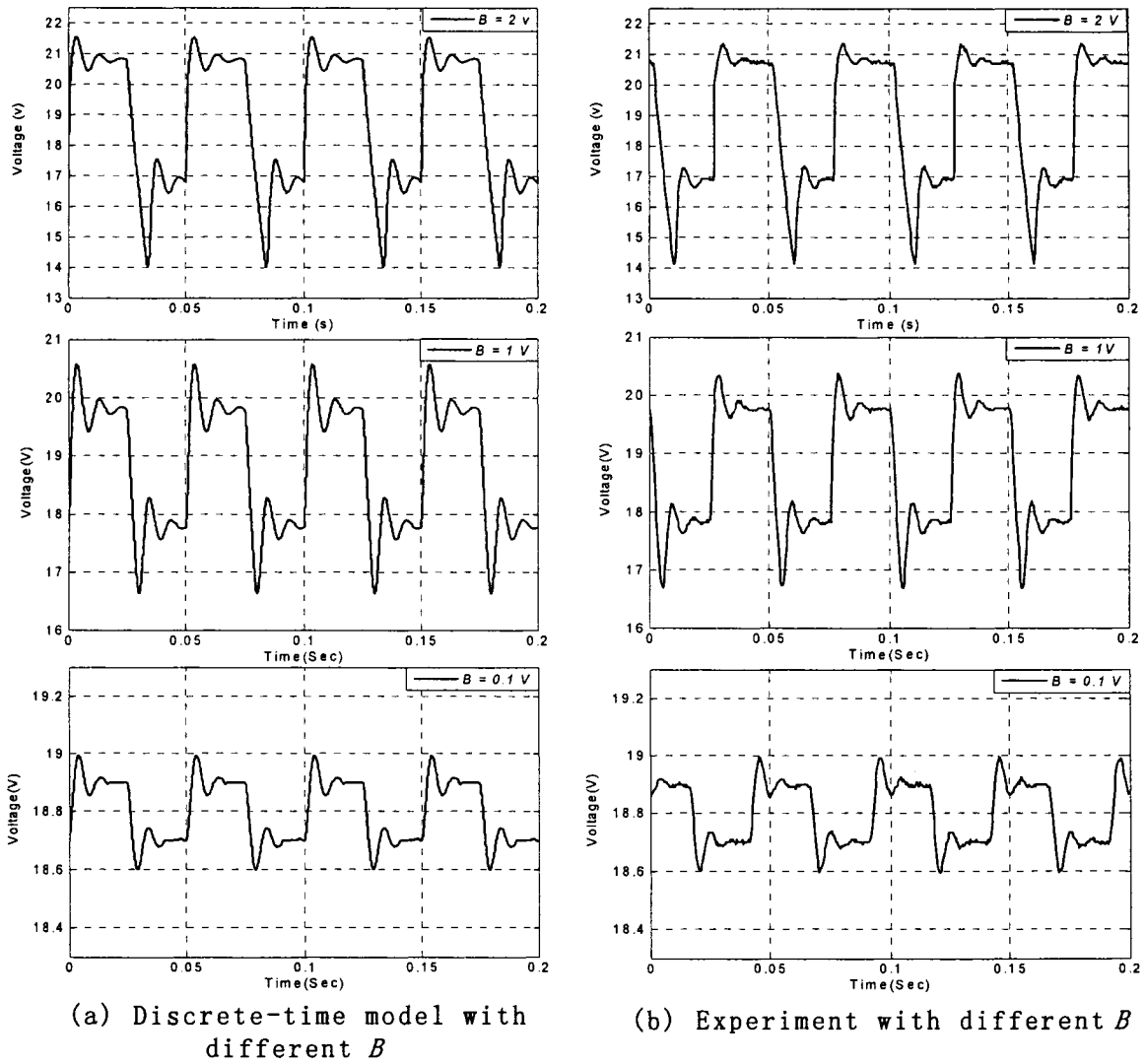
Figure 5-3: Closed-loop output-responses for discrete-time model and experiment with operating point $N2$.
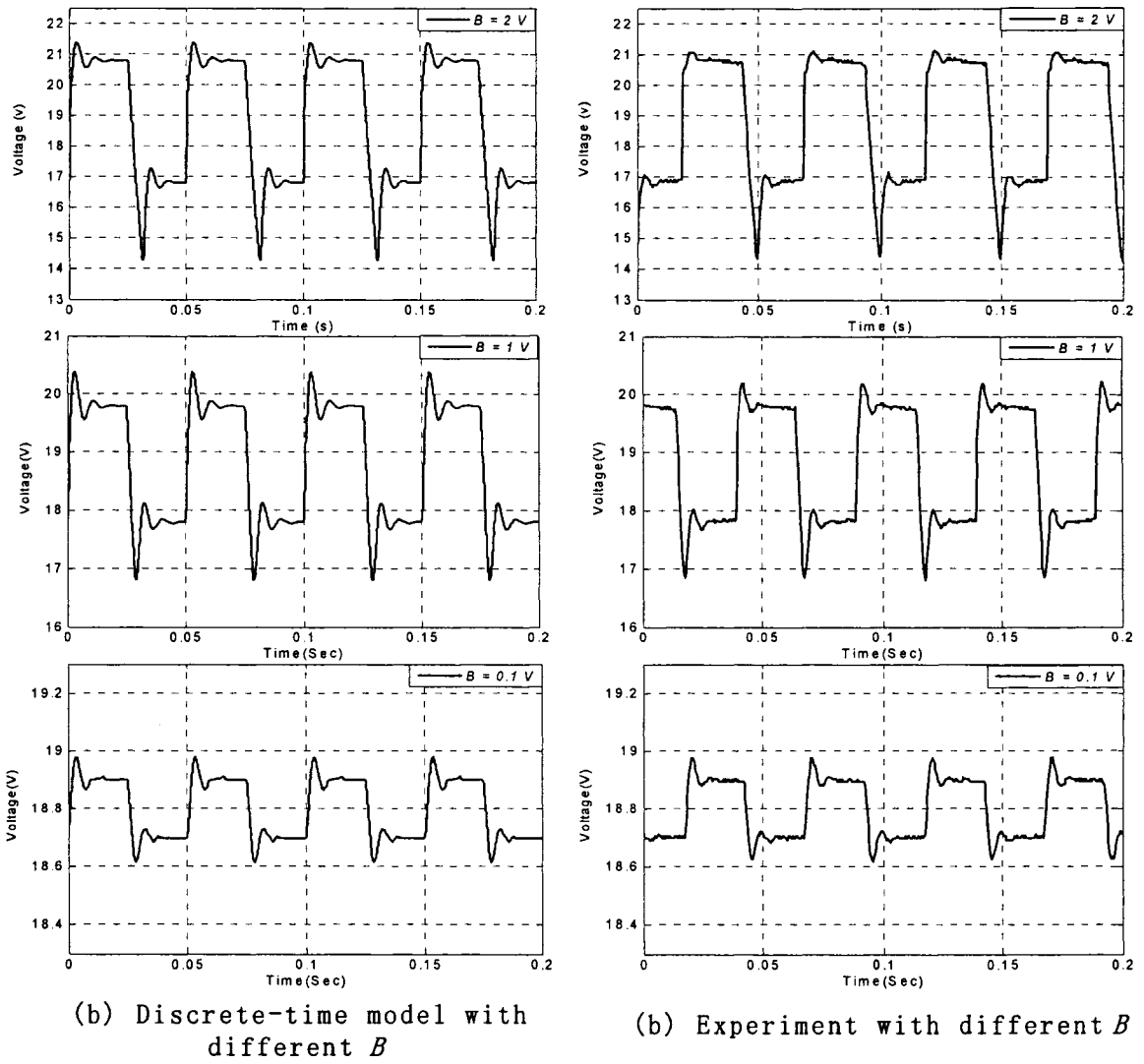
(b) Discrete-time model with
different B

(b) Experiment with different B

Figure 5-4: Closed-loop output-responses for discrete-time model and experiment with operating point $N3$.

55

Chapter 6

Future work and conclusion

6.1 Robust control design using a frequency response technique

The use of an appropriate model is central to the control design process in electronic circuits. An incomplete model may miss crucial aspects of system behavior and therefore lead to unsatisfactory controllers. In this thesis, a zero-order hold (ZOH) equivalent discrete time model of the boost converter for computing its small signal frequency-response and large signal and small signal closed-loop behavior over different operating points has been derived and experimentally confirmed. With this model, non-ideal effect and operation in both continuous and discontinuous current modes can be easily taken into account.

Table 6-1   Different operating points with constant output voltage V_o

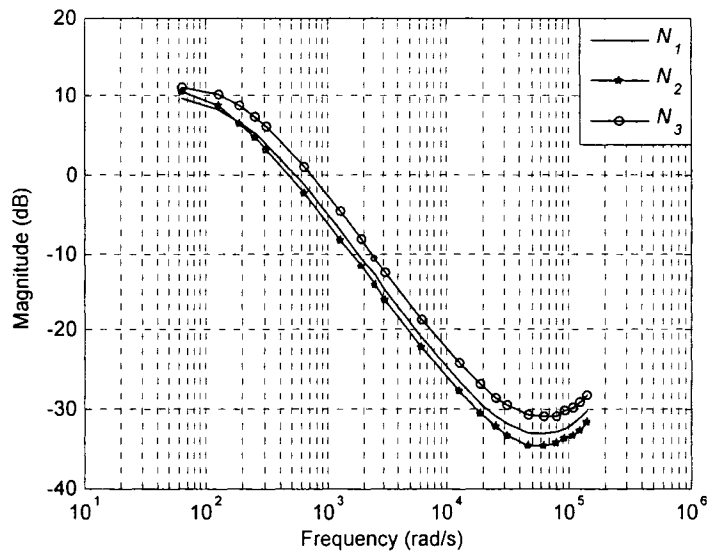| Operating pt	V_d (V)	R_{load} (Ω)	D	V_o (V)(open loop)
N_1	10	74.94	0.4	18.8
N_2	10	99.6	0.3452	18.8
N_3	12	74.94	0.2972	18.8

56

Figure 6-1: Magnitude response for discrete-time model with three different operating points.
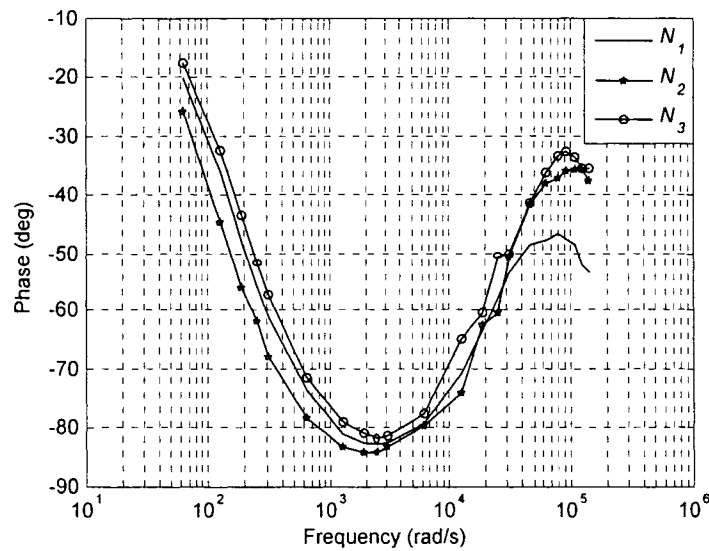

Figure 6-2: Phase response for discrete-time model with three different operating points.

57

In contrast to Section 5.1 where the frequency-response was obtained for constant DC input duty cycle rather than output voltage, the study of the small signal frequency-response on the basis of maintaining constant output voltage is more valuable for controller design point of view. With the intention of future robust control studies on the boost converter in discontinuous-conduction mode, an initial evaluation of the small signal frequency-response simulation predicted by the discrete-time model at different operating points (Table 6-1) based on keeping the output voltage of the boost converter always constant is presented in Figs. 6-1 and 6-2. The design of a robust controller for the boost converter using a frequency response technique to guarantee stability and performance over the entire operating range will be attempted in future work.

The robust controller design will be attempted along the line of [20] with guaranteed minimum gain margin and phase margin for the loop at all available operating data. The minimum gain and phase margin allowance is to ensure that if new operating ranges are encountered besides those considered in this work, the controller still has a cushion for loop stability. Due to time limitations, further investigation of this topic is future work emanating from this thesis.

6.2   Conclusion

In this thesis, a ZOH equivalent discrete-time modeling approach to the boost converter is studied from the point of view of computing steady-state behavior and the small signal frequency-response of the boost converter considering non-ideal components. The study has been experimentally verified. This discrete-time model is applicable to both continuous and discontinuous inductor current modes. The nonlinear transient behavior in the closed-loop induced by output voltage feedback PI controllers for such converters with 5% perturbation is studied with experimental results. It is shown that the results so obtained using the discrete-time model provide a reasonably good approximation to the experimental boost converter behavior, with and without feedback.

Bibliography

[1] T.M. Undeland, N. Mohan and W.P. Robbins, "Power Electronics: Converters, Applications, and Design", John Wiley and Sons, 2nd Edition 1995.

[2] R.D. Middlebrook and S. Cuk, "A general unified approach to modeling Switching-converter power stage", IEEE Power Electronics Specialists Conference Record, pp. 18-34, 1976.

[3] V. Vorperian, "Simplified analysis of PWM converters using model of PWM switch. Part I: Continuous conduction mode", IEEE Trans. Aerosp. and Electron. Syst., pp. 490-496, May, 1990.

[4] S. Cuk and R.D. Middlebrook, "A general unified approach to modeling Switching dc-to-dc converters in Discontinuous conduction mode", IEEE Power Electronics Specialists Conference (PESC), pp. 36-57, 1977.

[5] V. Vorperian, "Simplified analysis of PWM converters using model of PWM switch, Part II: Discontinuous conduction mode", IEEE Trans. Aerosp. and Electron. Syst., Vol. 26, pp. 497-505, May, 1990.

[6] A. Reatti and M.K. Kazimierczuk, "Small-signal model of PWM converters for discontinuous conduction mode and its application for boost converter", IEEE Trans. Circuits and system, Vol. 50, No. 1, pp. 65-73, Jan, 2003.

[7] D. Czarkowski and M.K. Kazimierczuk, "Energy-conservation approach to modeling PWM dc-dc converters", IEEE Trans. Aerosp. and Electron. Syst., Vol. 29, pp. 1059-1063, July, 1993.

[8] A. Reatti, "Steady-state analysis including parasitic components and switching losses of buck and boost dc-dc converters under any operating condition ", Int. J. Electron., Vol. 77, No. 5, pp. 679-702, 1994.

[9] M. Yektaii, "Modeling and Analysis of Limit Cycles in Buck Converters under PI Control", M. Sc. Eng. Thesis, Lakehead University, Canada, 2005.

[10] K. Ogata, "Modern Control Engineering", 4th Edition, Prentice hall, Inc, 2002.

[11] S. Chapra and R.P. Canale, "Numerical Methods for Engineers: with Programming and Software Applications", 3th Edition, McGraw-Hill, Inc., 1998.

[12] T.J. Aprille and T.N. Trick, "Steady-state analysis of nonlinear circuits with periodic inputs", Proc. IEEE, Vol. 60, No. 1, pp. 108-114, 1972.

[13] E.A. El-Bidweihy and K. Al-Badwaihy, "Steady-state analysis of static power converters", IEEE Tran. on Ind. Appl., Vol. IA-18, No. 4, pp. 405-410, 1982.

[14] D.G. Bedrosian and J. Vlach, "An accelerated steady-state method for networks with internally controlled switches", IEEE Trans. Circuits and Syst. I, Vol. 39, No. 7, pp. 520-530, July, 1992.

[15] D. Li and R. Tymerski, "Comparison of simulation algorithms for accelerated determination of periodic steady-state of switched networks", IEEE Trans. Ind. Electronics, Vol. 47, No. 6, pp. 1278-1285, 2000.

[16] V.A. Caliskan and G.C. Verghese, "Multifrequency Averaging of DC/DC Converters", IEEE Trans. Power Electronics, Vol. 14, No. 1, pp. 124-133, 1999.

[17] J.W. Van der Woude, W.L. de Koning and Y. Fuad, "On the Periodic Behaviour of PWM DC/DC Converters", IEEE Trans. Power Electronics, Vol. 17, No. 4, pp. 585-595, 2002.

[18] R.C. Wong, "Accelerated convergence to the steady-state solution of closed loop regulated switching mode systems as obtained through simulation", IEEE PESC Proceedings, pp. 682-692, 1987.

[19] Edward P. Cunningham, "Digital Filtering: An Introduction", Houghton Mifflin Company, 1992.

[20] K. Natarajan, "Robust PID controller design for hydroturbines", IEEE Trans. Energy Conversion, Vol. 20, No. 3, pp. 661-667, Sept, 2005.

[21] J.G. Kassakian, M.F. Schlecht and G.C. Verghese, "Principles of Power Electronics", Addison-Wesley Publishing Company, 1st edition 1991.

Appendix A

Frequency-response experimental setup

Experimental circuit to determine the frequency-response of the boost converter is given in Fig. A-1.

A.1   Calculation of parameters

The boost converter parameters are calculated for a maximum output voltage of 18.8V at 0.4A with the following specifications, using ideal boost converter equations as shown below.

Input voltage $V_d = 10$V

Output voltage $V_o = 18.8$V

Nominal duty cycle $D = 40\%$

Maximum output current $I_{o,\text{max}} = 0.4$A

Switching Frequency $f_s = 50$kHz

The converter is designed to be operating in discontinuous-conduction mode. So in Section 1.6, the inequality $I_o < I_{oB}$ should be satisfied. Using the above mentioned value

62

of $I_{o,\mathrm{max}}$ and (1.3) the inequality can be written as,

$$0.4 < \frac{T_s V_o}{2L} D(1 - D)^2$$

that yields a maximum value of the inductor L_{max}.

As long as $L < 67.68\mu\mathrm{H}$ for the boost converter with switching frequency $f_s = 50\mathrm{kHz}$, the converter would be in discontinuous-conduction mode.

Inductor value is selected to satisfy L_{max}. Assuming that all the ripple current component of the diode current i_D flows through the capacitor and its average value flows through the load resistor, the capacitor value is chosen to be a big value so that the ripple of the output can be reduced to be as small as possible. Table A-1 lists the chosen values for L and C and other parameters that are calculated for the boost converter circuit. In addition, the values of the non-ideal components considered in this thesis are chosen within the range specified for the components in the datasheet.

Table A-1:   Parameters of the boost converter

$L = 58.1\mu\mathrm{H}(\mathrm{MPP\ Core})$	$r_L(dc) = 0.3\Omega$
$C = 220\mu\mathrm{F}$	$r_{DS}(dc) = 0.065\Omega$
$V_d = 10\mathrm{V}$	$r_F(dc) = 0.102\Omega$
$V_o = 18.8\mathrm{V}$	$V_F(dc) = 1.2\mathrm{V}$
$D = 40\%$	$\widehat{V}_{st} = 10\mathrm{V}$
$f_s = 50\mathrm{kHz}$	$f_c = \frac{1}{2\pi\sqrt{LC}} = 1.41\mathrm{kHz}$

A.2 Inductor

All magnetic cores exhibit some degree of hysteresis in their $B - H$ characteristic. Permeability μ of a particular material is defined as the ratio of magnetic flux density B and the magnetic field intensity H, $(\mu = \frac{B}{H})$. Permeability of magnetic materials is not constant but varies as a nonlinear function of B (hysteresis behavior). One of the determining

63

factors in the type and value of an inductor is the permeability of the core material. If the core is made of linear magnetic material (i.e. with constant μ), the inductor value is constant, otherwise the inductor's value varies with current [21].

The inductor chosen for this experimental setup is a Talema SD series with MPP (Molypermalloy Powder) as core material. The use of MPP cores provides a highly stable inductance over a wide bias current range.

In the circuit model for the inductor, the DC resistance of the winding r_L was considered in series with the inductor.

A.3 Load resistance

For this experiment, four resistors of type IRC-PW5W, $300\Omega \pm 5\%$, were connected in parallel connection and used as a 75Ω fixed load with additional resistances switched in parallel to it to step-increase and decrease load. IRC-PW series are axial leaded power wirewound resistors manufactured by TT electronics. Their power rating is derated with the case temperature in IRC-PW5 datasheet. For instance, a 75Ω resistor with 18.8V across it, needs a power rating $P = V^2/R = 4.7$W. So four resistors with a rating of 5W of each in parallel connection withstand a maximum load power of 20W.

A.4 Circuit notes

In this section some practical notes about the circuit setup are mentioned. While setting up an experiment, these notes would make the work easier for determining reliable response of the system.

A.4.1 Wiring

In experimental setup wires are chosen as short as possible because long wires in the circuit increase noise, resistive power losses, and add stray inductance to the circuit.

64

The capacitor, diode, inductor and load resistor are therefore wired as close together as possible and thicker wires are used since they have smaller resistance.

A.4.2 Input power supply

Two 1000μF electrolytic capacitors were paralleled to the input power supply to reduce the ripple on V_d.

A.4.3 Gate resistor

Ringing is a common problem in any circuit with very fast rise or fall times. A 10Ω resistor in series with the output of the MOSFET driver is added to reduce the ringing. Although this reduces ringing, it also slightly increases the rise and fall times.

A.4.4 Bypassing

The rapid charging and discharging of the MOSFET gate capacitance requires very high current spikes from the power supply. For each IC in the circuit, the application information was followed according to datasheets and parallel combination of capacitors with low impedance over a wide frequency range was used. A 4.7μF tantalum capacitor in parallel with a low inductance 0.1μF capacitor is usually connected to power supplies of the circuit to diminish noise and handle high current spikes from the power supplies.

A.4.5 Power dissipation

Due to high switching rate, power will be dissipated on MOSFET. The MOSFET is mounted on a heat-sink.

A.5 Data collection

Data was collected through RS232 serial interface of the oscilloscope (Fluke PM3370B). The default acquisition length on the oscilloscope is 512 data points for each trace. It is possible to increase the length of a trace from 512 points up to a maximum of 8k points (without memories expansion) which is the setting used in these experiments. This results in a trace length of 16 screens, or 160 divisions. The sampling period depends on the main TIMEBASE of the oscilloscope. For example if the main TIMEBASE is 10ms the total time that data is collected will be 10ms $\times 160 = 1.6$s and the sampling period will be $\frac{1.6}{8000} = 0.2$ms.

A.5.1 Magnitude calculation

The magnitude of the frequency-response is calculated by taking the FFT of the collected input and output data. Considering the number of samples taken through the oscilloscope is $N = 8$k, the sampling rate T for each frequency should be chosen so that the frequency under study is an integer multiple of the FFT frequency resolution $\frac{1}{NT}$, otherwise leakage in the desired frequency vector will lead to incorrect values.

A.5.2 Phase shift calculation

For measurement of phase shift between the input signal and the output signal of the circuit, they were connected on the two channels of the oscilloscope respectively. Although input and output data were not collected at the same time by the scope, the error checked with exactly same signal collected simultaneously on the two channels of the oscilloscope in analog mode, is verified to be so small that it can be neglected. Since the 8k acquisition memory is shared between the two channels, the maximum acquisition length for each trace can only now be 4k points for the oscilloscope used in experiment. Likewise, phase shift can be calculated using FFT. It is also noted that a low-pass digital Butterworth filter is essential due to the presence of ripple and noise in the experimental

66

system. The smallness of the amplitude of the input sinusoidal signal $A = 0.1V$ is the main source of the error, which makes considerable difficulty in measuring the phase response accurately.

A.6   Efficiency

Considering the discussion in the previous sections, the power conversion efficiency of the boost converter is calculated for the open-loop situation. The power efficiency of the experimental boost converter is given in Table A-2. In closed-loop case, the circuit efficiency is slightly less than the given value and is dependent on controller gains. It is also found that the efficiency of this boost converter in discontinuous-conduction mode decreases with increasing inductor current.

Table A-2: Efficiency of this experimental boost converter

	V_i	I_i	V_o	I_o	Efficiency
Boost converter	10.02V	0.542A	18.816V	0.254A	88%
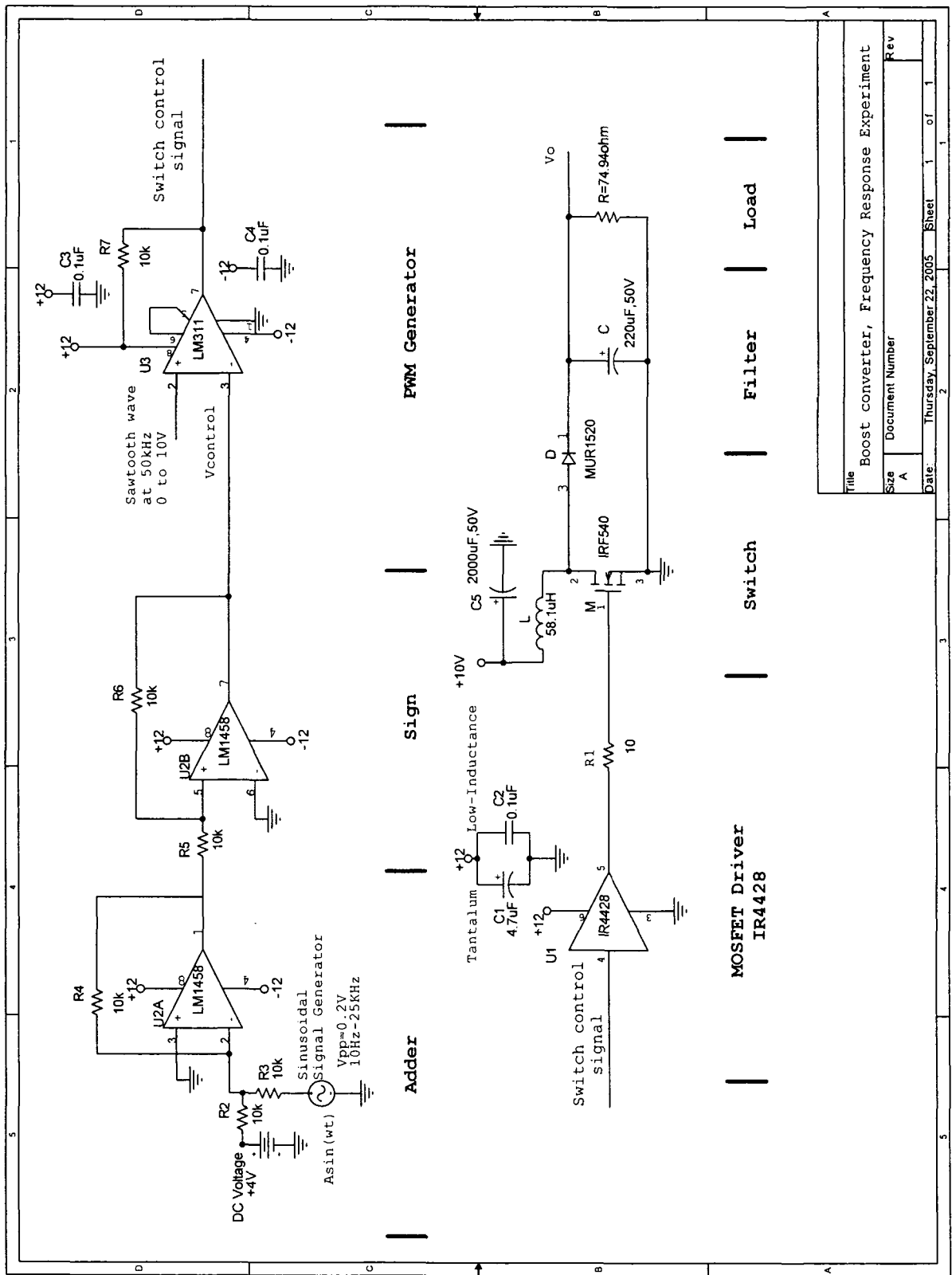
67

Figure A-1: Boost - experimental setup for frequency-response

68

Appendix B

Closed-loop experimental setup

Experimental circuit to predict the closed-loop output-response of the boost converter is given in Fig. B-1.

B.1 Subtraction circuit

The subtraction circuit used in the experimental setup is designed such that,

$$e = 2 \times R - V_o \tag{B.1}$$

where e is the error signal sent to the input of the PI controller for desired control signal and the value of R is half of the instantaneous value of the square-wave set-point trajectory.

B.2 Controller circuit

The feedback control system is designed to maintain the output voltage at V_{ref}. A simple PI controller with the following form is used to implement this closed-loop operation,

$$G_c(s) = K_p + \frac{K_i}{s}$$

69

with

$$K_p = \frac{x_1}{9.819\mathrm{k}\Omega}$$

$$K_i = \frac{1}{0.096\mu F \times x_2}$$

where x_1 and x_2 are the values of potentiometer $pot1$ and $pot2$ in kΩ which are adjusted to provide K_p and K_i gains respectively.

A particular setting of proportional gain K_p and integral gain K_i is chosen as 0.4 and 1000 per sec respectively.

B.3 Data collection

For closed-loop behavior, the main TIMEBASE is chosen as 20ms/Div and the acquisition length of this output trace is 4k data points which results in a trace length of 8 screens, or 80 divisions. The total time that data is collected is 20ms/Div×80 = 1.6s and the sampling period is $\frac{1.6}{4000}$ = 0.4ms. Hence, the closed-loop output-response captured from the experimental setup does not show the ripple between the switching period (T_s = 20μs).
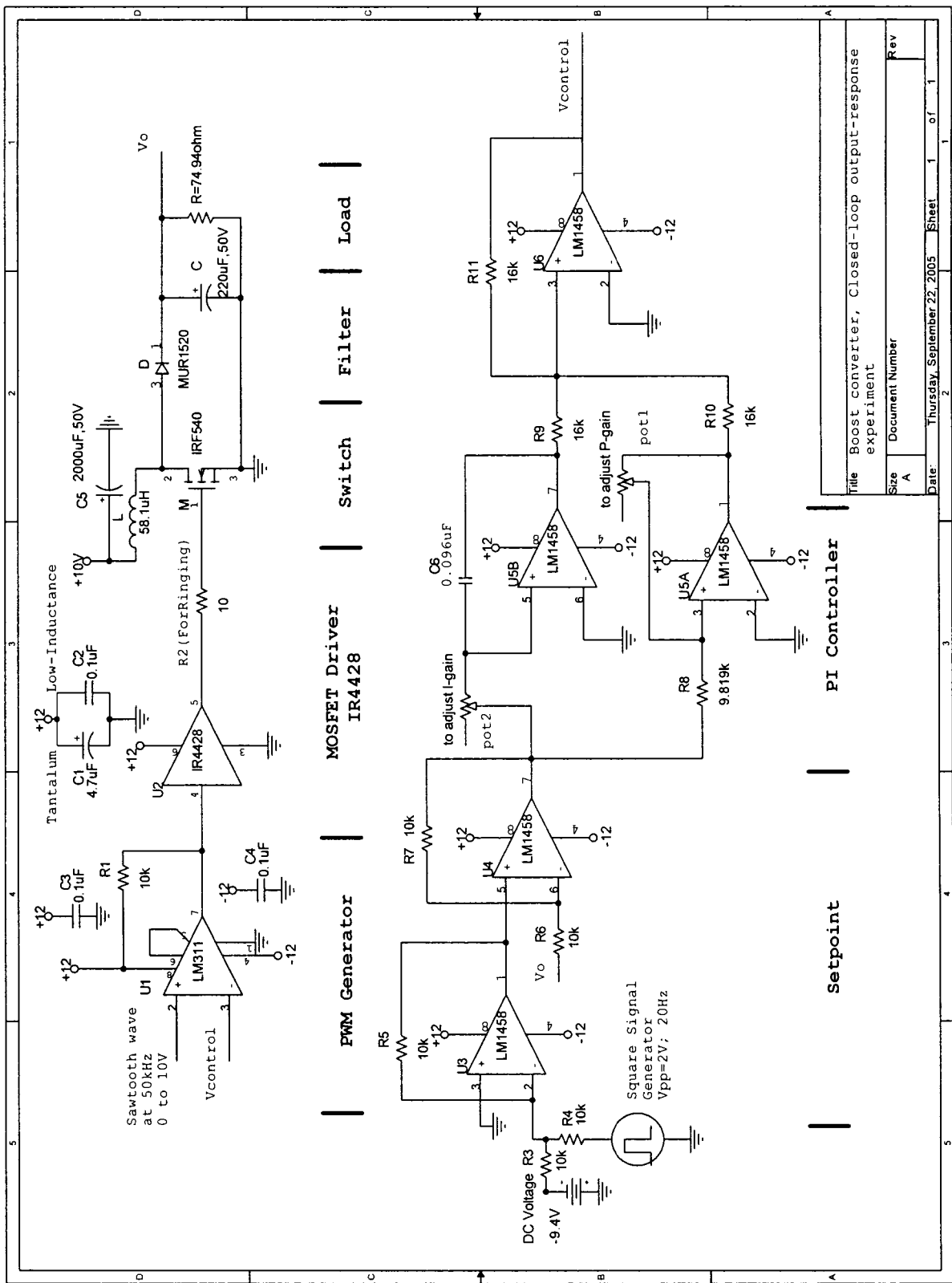
70

Figure B-1: Boost - experimental setup for closed-loop behavior

71